Title
Strain Fields Around Strain-Concentrating Features in Oxide Composites

Author
Samuel, Avery

Publication Date
2019

UNIVERSITY OF CALIFORNIA

Santa Barbara

Strain Fields Around Strain-Concentrating Features in Oxide Composites

A thesis submitted in partial satisfaction of the
requirements for the degree Master of Science
in Materials

by

Avery Francis Samuel

Committee in charge:
Professor Frank W. Zok, Chair
Professor Carlos G. Levi
Professor Daniel S. Gianola

March 2019

The thesis of Avery Samuel is approved.

Carlos G. Levi

Daniel S. Gianola

Frank W. Zok, Committee Chair

March 2019

ABSTRACT

Strain Fields Around Strain-Concentrating Features in Oxide Composites

by

Avery Francis Samuel

Inelastic straining in the vicinity of strain-concentrating features in fiber-reinforced ceramic composites mitigates the high stresses that would otherwise be present and therefore alters the local conditions required to initiate fracture. The present study examines such effects through experimental measurements of strain fields around holes and notches in two oxide composites coupled with finite element simulations based on an inelastic constitutive model for the composite response. Computed strains fall within the bounds of experimental measurements for open-hole tension over most of the loading history. The results motivate a fracture criterion based on attainment of a critical combination of normal strain and shear strain over a characteristic area at the edge of the hole or notch. The response of single edge-notched tensile specimens proves to be more challenging; because of the finite bending stiffness of the loading train, the boundary conditions on the test specimens evolve during loading, with bending playing an increasingly important role as the applied load is increased.

Table of Contents

1. Introduction

Fiber-reinforced ceramic matrix composites (CMCs) of practical interest possess a capacity for inelastic straining prior to ultimate failure. Inelasticity arises through combinations of matrix microcracking, interfacial debonding and sliding, and fiber fracture. It facilitates redistribution of stresses around strain-concentrating features, leading to more robust structural response[1–4]. Accurate modeling of inelasticity in CMCs is expected to enable designs of engineering components that are less conservative than those which emerge from purely elastic analyses. The present study addresses issues in modeling inelasticity and failure in one particular class of CMCs.

Approaches to modeling inelastic deformation of CMCs fall into one of three broad categories: micromechanics, continuum damage mechanics (CDM), and phenomenological plasticity[3–8]. Micromechanical approaches attempt to relate constituent properties and microstructural characteristics with the physical mechanisms underlying inelasticity. An exhaustive suite of micromechanical models has been developed to describe matrix cracking and interfacial debonding and sliding in *unidirectional* composites under simple stress states (*e.g.* uniaxial tension, pure shear)[9–13] and tunnel cracks in off-axis plies of cross-ply laminates[14]. But these models are difficult to generalize to arbitrary multiaxial stress states and to account for microstructural heterogeneities that naturally arise in most CMCs[3]. Approaches based on CDM provide greater flexibility and are ostensibly able to capture a multitude of phenomena without explicit information about the mechanisms involved. CDM uses state variables to represent effects of damage on macroscopic response and conjugate thermodynamic forces that govern damage growth. Extensive experimental data are usually required to calibrate the models[3,5]. Phenomenological plasticity models are also able to capture the effects of damage while being simpler than those based on CDM. They employ macroscopic stress-strain data obtained from standard mechanical tests and interpreted within a continuum deformation framework (though generally not one based on metal plasticity). These require fewer experiments for calibration than CDM approaches and represent the first step in progressing beyond purely elastic analyses[3].

Prediction of load-bearing capacity and failure of CMC structures is invariably more challenging than prediction of deformation alone. Two problems arise. The first involves *strain gradients*, as exemplified by beam bending. Under pure bending, strains vary linearly across the beam width, and the stresses are unidirectional and aligned with the beam axis. If the beam is made of a unidirectionally-reinforced CMC with fibers aligned with the beam axis and with interfaces sufficiently weak to enable global load sharing, its load-bearing capacity can be predicted on the basis of the stress-strain response of the fragmenting fiber array and Euler-Bernoulli beam theory[12]. Because of the nature of the stress-strain response of a fragmenting fiber bundle – one of gradual reduction in tangent modulus with increasing stress, attainment of a stress maximum, and subsequent gradual softening – the nominal bending strength calculated from the maximum bending moment is usually significantly greater than the uniaxial tensile strength of the fiber bundle itself. The enhancement arises from a combination of: (i) the stress re-distribution associated with the non-linear fiber bundle response and (ii) the fact that the bending moment can continue to rise as the stress on the fibers on the outer face of the beam exceed the fiber bundle strength and gradually soften. One of the implications is that the failure strain measured on the tensile face would exceed that measured from a uniaxial tensile test, because the latter test does not exploit the post load-maximum domain. This is a straightforward example where structural failure – based on a limit or collapse load – cannot be predicted solely on the basis of the uniaxial tensile strength or failure strain.

The second issue involves *multiaxial loading*. For 2-dimensional CMC structures loaded uniformly, there is some prospect that the failure loads could be predicted from the failure stresses measured in a few standard mechanical tests in combination with a Hill-type failure criterion (*e.g.* Tsai-Hill[15] or Tsai-Wu[16]). In contrast, when stresses are distributed *non-uniformly* through the structure, failure prediction becomes even more challenging. Estimates can be obtained by identifying the macroscopic stresses at which the most heavily-stressed element in the structure reaches criticality, using failure stresses or strains measured from standard tests in defining failure initiation. But the resulting predictions are invariably conservative and may not be particularly useful in engineering design[1,3,17]. The discrepancies often arise because the volumes of material experiencing the highest stresses are small and hence the local conditions required for criticality differ from those in standard (large-volume) test specimens. This phenomenon invariably leads to *size-dependent strength*. There has been some success in capturing these effects in notched and open-hole tensile geometries, through numerical analyses or approximate analytical solutions for the stress/strain fields in combination with failure criteria based, for example, on attainment of a critical tensile stress over a characteristic length scale[1,4–8,18]. But the path to extending the failure parameters inferred from one test configuration to another is not evident. Indeed, one would almost certainly expect the local conditions at failure to depend sensitively on the nature of the stress and strain states both globally and locally.

More sophisticated modeling approaches based on cohesive zone concepts within a finite element framework can be used to address structural stability following localization and macroscopic crack formation. In principle, the traction laws defining the cohesive zone can include both normal and shear tractions of almost any form. The main drawback of these approaches is their high computational cost[19–21].

The present study is concerned with evaluating the capabilities of a model for inelasticity of the third type discussed: a plasticity-like approach based on deformation theory. The model has been used previously in conjunction with studies on strain distributions of open-hole tensile specimens of a SiC/SiCN CMC[3]. There, good agreement had been obtained between computed and measured strain fields over most of the loading history. The primary objective of the present study is to assess the utility of the model in predicting strain fields in all-oxide CMCs containing strain-concentrating features. In addition, an attempt to glean insight into the conditions required for fracture is made through the application of a new failure criterion.

The remainder of this thesis proceeds as follows. First, overviews of materials, test procedures, constitutive models and model calibration are presented. Second, the results of mechanical tests (uniaxial tension in 0°/90°, ±45° and 15°/75° orientations, and Iosipescu shear) used to calibrate the constitutive models for two all-oxide CMCs of this study are presented. Third, the capabilities of the model are assessed through comparison of measured and computed displacements and strain fields in tensile specimens containing either an open hole or a single edge notch. Motivated by results of these simulations, the effects of the boundary conditions on the predictions of this model are investigated. Finally, a rudimentary failure criterion based on local normal and shear strains along with a characteristic area in the most heavily strained regions is proposed. Appendices A and B, respectively, present refinements to the procedures used to calibrate the model and an examination of the influence of the terminal values of the calibration curve inputs on the predicted strain distributions.

2. Materials and Analysis Methods

2.1. Materials

Two all-oxide composites were used in this study. Both utilize the porous-matrix concept[20] to enable damage tolerance and thus the fibers are uncoated. The first, designated here as M1, comprises 3M Nextel 610 alumina fibers in an 8-harness satin weave and a matrix of 85% Al_2O_3 + 15% 3YSZ. The material was manufactured via slurry infiltration of the matrix into desized fiber cloths, followed by lay-up, drying and firing (Pritzkow Spezialkeramik, Filderstadt-Sielmingen, Germany). The panels were 2.9 mm thick and had a fiber volume fraction of 39%. The matrix between tows is inhomogeneous in composition and structure. In addition to the characteristic fine-scale porosity necessary for damage tolerance, residual pores exist both within and between the tows, evidently a result of incomplete slurry infiltration (Figure 1A). Such features are commonly found in this class of composite, albeit not usually to the extent seen here. The second material, designated M2, comprises 3M Nextel 720 alumina-mullite fibers in an 8-harness satin weave with a matrix of 100% Al_2O_3, also manufactured via slurry infiltration (Siemens, Munich, Germany). The panels were 3.0 mm thick and had fiber volume fraction of 41%. Microstructural heterogeneities in this material are similar to those of the first material (Figure 1B).

2.2. Mechanical testing procedures

In order to calibrate and define the constitutive models used in FE simulations, four types of mechanical tests were conducted on each material: uniaxial tension with fibers in the 0°/90°, ±45°, and 15°/75° orientations, and Iosipescu shear (ASTM 5379) with fibers in the 0°/90° orientation. Two additional types of tests were used for assessment: open-hole tension and single edge-notched tension (insets in Figure 1), both with fibers in the 0°/90° orientation. Two notch lengths were used for edge-notched tension. Two or three specimens were typically used for each test type. In all tension tests, load was applied using a servohydraulic test frame (Material Test System 810, MTS, Eden Prairie, MN, USA), and fiberglass tabs were used to promote even load transfer and to prevent crushing of the specimen ends by the hydraulic wedge grips. Shear tests utilized a standard Iosipescu test fixture (Wyoming Test Fixtures, Inc., Salt Lake City, UT, USA).

The external boundaries of all test samples were cut by laser machining. The samples used in unnotched tension tests had dogbone geometry with gauge dimensions of 10 mm wide by 25 mm long. The specimens for open-hole tension and edge-notched tension were rectangular with widths of 25 mm and gauge lengths of about 50 mm. Holes of the open-hole tension specimens were centered along the length and width of the test coupons. Small initial holes were bored out to a diameter of 7.5 mm (yielding a diameter/gauge width ratio of $a/W = 0.3$). Notches for edge-notched tension were centered along the specimen length. They were cut to depths of 7.5 and 12.5 mm (notch length/gauge width ratios of $a/W = 0.3$ and 0.5) with a diamond wafering blade on a surface grinder. The width of the notches was approximately 0.7 mm. The specimens for the Iosipescu shear tests used a geometry similar to that described in ASTM D3579, but with a notch angle of 105° rather than 90° to reduce transverse stresses in the central ligament[3].

Deformation fields were measured using 3D digital image correlation (DIC) (VIC-3D, Correlated Solutions, Inc., Irmo, SC, USA), following procedures detailed elsewhere[3]. Notable analysis parameters include an image scale factor of ~12 μm/px and a subset size for image correlation of 31 – 45 px (350 μm – 500 μm). Iosipescu test specimens were additionally instrumented with 0°/90° stacked strain gauge rosettes (CEA-13-062WT-120, Vishay Micro Measurements, Wendell, NC, USA) oriented at ±45° to the specimen axes on one surface.

Reported strains for the uniaxial tension tests are average readings from 5 equally-spaced parallel virtual extensometers in either the longitudinal or transverse orientation. Reported strains of the Iosipescu tests are averages of the front-face DIC strain (calculated using an area-average over the central ligament) and the back-face strains measured with the strain gauges. The results of each test type were eventually averaged to produce a single stress/strain curve for use with the inelastic constitutive model. Data beyond the load maxima were excluded from the analysis.

2.3. Inelastic constitutive model

In this study, inelasticity is modeled using a phenomenological model based on deformation theory of plasticity developed during previous studies on SiC CMCs[3]. Briefly, the model relates in-plane strains, ε_1, ε_2 and γ_{12}, to corresponding stresses σ_1, σ_2 and τ_{12} (with 1 and 2 being the two fiber directions), through an effective compliance matrix of the form

$$\begin{bmatrix} \varepsilon_1 \\ \varepsilon_2 \\ \gamma_{12} \end{bmatrix} = \begin{bmatrix} \frac{\varepsilon_0(\bar{\sigma}/C_0)}{\bar{\sigma}/C_0} & \frac{\varepsilon_{0T}(\bar{\sigma}/C_0)}{\bar{\sigma}/C_0} & 0 \\ \frac{\varepsilon_{0T}(\bar{\sigma}/C_0)}{\bar{\sigma}/C_0} & \frac{\varepsilon_0(\bar{\sigma}/C_0)}{\bar{\sigma}/C_0} & 0 \\ 0 & 0 & \frac{\gamma_s(\bar{\sigma}/C_s)}{\bar{\sigma}/C_s} \end{bmatrix} \begin{bmatrix} \sigma_1 \\ \sigma_2 \\ \tau_{12} \end{bmatrix}. \tag{1}$$

Here ε_0 and ε_{0T} are axial and transverse strains as functions of axial stress in a tensile test in the 0°/90° orientation, γ_s is the shear strain in a 0°/90° shear test, $\overline{\sigma}$ is a Hill-type effective stress, defined by

$$\overline{\sigma} = \sqrt{C_0^2(\sigma_1 - \sigma_2)^2 + (4C_{45}^2 - C_s^2)\sigma_1\sigma_2 + C_s^2\tau_{12}^2} \tag{2}$$

and C_0, C_s, and C_{45} are constants determined through calibration. The latter constants nominally relate the stresses at the onset of nonlinearity for 0°/90° tension (σ_0), pure shear (τ_0) and ±45° tension (σ_{45}), via $C_0\sigma_0 = C_s\tau_0 = C_{45}\sigma_{45}$. One of the constants, C_0, is arbitrarily set to 1. The model assumes plane stress, cubic in-plane symmetry of composite properties, monotonic and proportional loading, and no shear/normal coupling[3].

2.4. Model calibration

The constants C_{45} and C_s were determined by two least-squares regression steps. The first is based on the predicted relationship between the responses in ±45° tensile tests and Iosipescu shear tests. To obtain this relationship, the stress of the ±45° tensile test is transformed from the global coordinate system to one defined by the fiber axes, strains are obtained from the compliance matrix, and the strains are then transformed back into the global coordinate system. The resulting relationship between the strains of the two tests is:

$$\varepsilon_{45}(\sigma) - \varepsilon_{45T}(\sigma) = \frac{C_s}{2C_{45}}\gamma_s\left(\frac{C_{45}}{C_s}\sigma\right). \tag{3}$$

where ε_{45} and ε_{45T} are axial and transverse strains in the ±45° tension test. This operation sets the ratio of C_s/C_{45}. The second step sets C_s and C_{45} to specific values using a relationship based on the axial response in 15°/75° tension. Through an analogous process of stress and strain transformations, the measured and predicted tensile strains are found to be related by:

$$\varepsilon_A(\sigma) = \frac{C_0}{8\overline{C}}\left[7\varepsilon_0\left(\frac{\overline{C}}{C_0}\sigma\right) + \varepsilon_{0T}\left(\frac{\overline{C}}{C_0}\sigma\right)\right] + \frac{C_s}{16\overline{C}}\gamma_s\left(\frac{\overline{C}}{C_s}\sigma\right); \qquad \overline{C} = \frac{1}{2}\sqrt{3C_0^2 + C_{45}^2} \tag{4}$$

where ε_A is the axial strain in the 15°/75° test. (This calibration procedure differs from that employed in previous studies[3]. That method did not accurately define the constitutive model, as described in Appendix A. Notwithstanding, the values obtained with the method here fall within the range of those expected from the procedure of the previous studies.)

2.5. Finite element model

Finite element (FE) simulations were performed with ABAQUS standard (version 6.16, Dassault Systèmes, Vélizy-Villacoublay, France). The maximum stress for each simulation was twice the corresponding measured failure stress in the experiments for that type of test. For comparison with experimental data, displacements (U and V) of every node in the model were extracted at 10 MPa increments in net-section stress. Simulations of open-hole tension utilized a quarter-symmetry FE model with four-node, quadrilateral, plane-stress elements. Displacement was applied monotonically at the top boundary in the +Y direction[3]. Simulations of edge-notched tension tests used half-symmetry models with eight-node, quadrilateral, plane-stress elements. For the majority of simulations of edge-notched tension in this work, monotonic uniform *displacement* was applied on the bottom boundary in the -Y direction.

Section 3.6 examines the effects of a monotonic uniform *stress* applied to the bottom boundary in the -Y direction. When applicable, the former condition is indicated by Δ and the latter by σ. Omission of both indicates the uniform displacement condition.

The inelastic model is implemented via a UMAT subroutine. Inputs to the UMAT are the functions ε_0, ε_{0T}, and γ_s, and the calibration constants C_0, C_s, and C_{45} (Table 1). (The terminal values of these strain functions can have a pronounced effect on the predictions of this model. A preliminary investigation into these effects is given in Appendix B.) In order to glean insight into the role of inelasticity, a parallel set of computations was performed assuming the material to be elastic with Young's modulus E_y parallel to the fiber directions, in-plane shear modulus, G_{xy}, and in-plane Poisson's ratio, ν_{xy}. The elastic constants for both materials, obtained from 0°/90° tensile and Iosipescu shear tests, are given in Table 2.

2.6. Comparison methods

Comparisons between numerical simulations and experimental measurements are made on the bases of both global and local responses. For open-hole tension, global response is characterized by the variation in net-section stress with hole strain, where hole strain is defined as the ratio of axial displacement across the centerline of the hole to the initial hole diameter (see inset in Figure 3A). For notched tension, global response is couched in terms of the net-section stress and the near-tip axial displacement, the latter obtained over a 20 mm-long virtual extensometer placed 1 mm ahead of the notch tip (inset in Figure 3C).

Local responses are based on spatial distributions of shear strain, γ_{xy}, and axial tensile strain, ε_{yy}, in the vicinity of notches and holes, computed as follows. Scattered displacement data from DIC and FEA were interpolated in x and y with Delaunay triangulation and then evaluated on a common grid of evenly-spaced (x, y) coordinates. Strains were computed by central differencing of the displacements on the common grid with respect to spatial coordinates. The strains were then averaged using a Gaussian filter. The filter length, h_f, has the physical meaning of gauge length for strain computation. A value of $h_f = 2$ mm was used, selected in part to smooth out short-range strain fluctuations associated with the tows (each about 1 mm wide). The standard deviation for the filter was set to $0.25h_f$. Results are presented as contour plots of axial and shear strains at two representative stress levels: one at 2/3 of the failure stress and another close to but slightly below the failure stress (within 5-10 MPa).

Strains are also compared on the basis of line scans near the holes and notches. Shear strains were averaged over 1 mm-wide vertical bands (parallel to the loading direction) just ahead of the hole or notch edge (see insets in Figures 4A, 6A, and 8A). The signs of the averaged values are omitted so that only the *magnitudes* are compared. In addition, the reference position in the vertical direction is the midplane of the sample rather than one end of the gauge section. The bands pass through the primary feature of these strain distributions, namely lobes of high shear strain. Similarly, scans of axial strains were averaged over 1 mm-wide bands along horizontal lines emanating from the hole or notch edge (insets in Figures 5A, 7A, and 9A). For these lines, the signs of the strains are retained. The vertical position of such lines corresponds approximately to the plane of minimum cross-section. (In some cases, these lines were shifted slightly to coincide with those at which the axial strains persisted to the greatest horizontal extent; because of slight asymmetry in the strain fields, the locations of the latter lines differ slightly from those of minimum cross-section.)

3. Results and Analyses

3.1. Mechanical tests for model calibration

In 0°/90° unnotched tension, M1 is stiffer and stronger than M2, but has a lower failure strain (Figure 2). The response in this orientation for both materials is approximately bi-linear, with the transitions occurring over the stress range of 50 to 100 MPa for M1 and 25 to 75 MPa for M2. The higher stresses of the transition for M1 indicates that the initial matrix cracking stress is higher. The final tangent moduli are ~70 and 42 GPa for M1 and M2, respectively. These values are about 25% and 40% lower than the corresponding initial values. Assuming that the axial fibers are perfectly aligned and that they bear all incremental loads shortly before failure, the final tangent moduli are expected to be 72 and 50 GPa for M1 and M2, comparable to the measured values. The curves for 15°/75° and ±45° tension and for pure shear exhibit progressively larger reductions in tangent moduli with increasing strain, reflecting the increased role of the matrix in these responses. Comparisons of the measured stress-strain curves with those computed from the calibrated constitutive model show the internal self-consistency of the calibrated model, i.e. that the expected stress-strain relationships of the model hold with the calibration constants found (Figure 2). (See Appendix A for a discussion of when this may not be the case.)

3.2. Open-hole tension tests

The macroscopic responses for open-hole tension, both measured and computed and for both materials, are linear at low stresses, to about 60 MPa for material M1 and 30 MPa for M2 (Figures 3A and 3B). These stresses represent about 40% and 25% of the respective failure strengths. The stiffnesses of the computed responses from both elastic and inelastic material models match the experimental values in this regime. Higher stresses are accompanied by macroscopic nonlinearity in the measured responses, with progressive reductions in tangent moduli. The macroscopic response appears to be captured well by the FE simulations with the inelastic constitutive model but not (unsurprisingly) with the elastic model. At the fracture stress the inelastic hole strains are about 20% (M1) and 40% (M2) of the respective total strains.

The full field *shear strains* contain qualitatively similar features across materials and models. Lobes of high shear strain (up to ~0.004 in both materials) oriented along the loading direction develop at the edges of the holes (Figure 4). These regions intensify in strain and expand in size along the loading direction with increasing stress. The shapes of the lobes from both models are similar to those of the measured fields, although those from the inelastic model show a better quantitative match with the experimental results. (The figures include full-field strains from the experimental measurements and FE simulations with the inelastic model. For simulations with the elastic model, only the line scans are shown.) In M1, the measured elevation varies across lobes within and between samples, some exhibiting elevations twice those of others. These differences and the resulting asymmetries in the strain fields naturally are not captured by the present finite element simulations, because of the imposed symmetry.

Individual line scans of the shear strains (measured and computed) exhibit a consistent overall pattern. With increasing vertical distance from the sample midplane, the strain magnitude increases to a peak, decreases to a local minimum, rises to a second (lower) peak, and then decays (Figure 4). However, the magnitudes of the measured strains can differ considerably from one lobe to the next, even within a single test specimen. These variations are confounded by short-range fluctuations associated with the underlying tow architecture. (These fluctuations are significantly reduced relative to those in the raw data but nevertheless persist even following area-averaging.) As expected, strains from the elastic model are smaller than those of the inelastic model. The largest differences between these predicted values occurs at the first peak and at the fracture stress, at which point the ratios of peak strains from the two models range from about 2 to 4. All lines of a given sample converge at large distances from the midplane. For material M1, the predictions from the inelastic model fall near the middle of the full range of measured strains over the entire gauge length. The latter range is indicated approximately by the shading in Figure 4. The elastic model predicts strain magnitudes that fall near the lower end of the measured range (though these predictions are also within the range for the entire gauge length). For material M2, the computed strains of the inelastic model show a somewhat weaker correspondence with the measured values, consistently falling near the lower end of the measured range. Strains computed with the elastic model are generally below the measured values. Finally, the peak (measured) shear strains at the fracture stress of 0.004 (M1) and 0.007 (M2) are roughly half as large as and equal to, respectively, the failure strains measured in the Iosipescu shear tests.

The full-field *tensile strains* show elevations on either side of the holes and nearly strain-free regions above and below the holes, as expected (Figure 5). The highly-strained regions intensify and expand radially as stress increases. The largest tensile strains are distributed around the hole over a region subtended by radial arcs about ±35° to the horizontal midplane. The largest measured strains and subsequent failure locations often occurred at the edges of this range (*i.e.*, at around +35° or -35° from horizontal) rather than along the plane of minimum cross-section. Sample-to-sample differences in the locations of greatest strain are attributed to variation in local fiber placement and microstructure.

The line scans of the tensile strains exhibit a single peak at the edges of the holes and decay with increasing distance. In contrast to the scatter found in the line scans of shear strains, the tensile strains fall within a rather narrow range (Figure 5). The magnitudes of strains predicted by the inelastic model generally fall within the range of experimental values, with the exception of the most heavily strained regions near the hole edge very near the failure stress. The elastic predictions, in contrast, are consistently near or below the lower end of the experimental range. The strains near the hole at the fracture stress exceed the failure strains measured in uniaxial tension tests, over distances of about 2 mm.

3.3. ***Edge-notched tension tests (a/W = 0.3)***

The macroscopic responses for edge-notched tension tests, measured and computed and for both materials, are linear until 30 MPa for M1 and 20 MPa for M2 (Figures 3C and 3D). These correspond to 35% and 25% of their failure strengths. The stiffnesses of the computed responses for both material models match the experimental values in this regime. Higher stresses produce macroscopic nonlinearity and progressively decreasing tangent moduli in the measured responses. The inelastic deformation is partially captured by the inelastic constitutive model (and again not by the elastic model). At fracture, the total displacements predicted by the inelastic model are around 70% (M1) and 65% (M2) of the measured values, with the inelastic contributions being about 10% (M1) and 25% (M2) of those computed total displacements. (Note that this section concerns the elastic model and the inelastic model with the displacement Δ condition.)

The *shear strain* fields exhibit concentrated lobes (up to 0.004 in M1 and 0.006 in M2) emanating from the notch tips (similar to those seen around open holes). These lobes grow parallel to the loading direction with increasing stress (Figure 6). The shapes of the lobes from both models are similar to those of the measured fields, although the strain magnitudes in lobes from the inelastic model exhibit better quantitative match with the measurements for both materials. The discrepancies between the inelastic model and the measurements are larger for M2 than for M1. In the figures, the lobes appear to begin behind the tips of the notches. This is because DIC cannot correlate near edges where the subsets are incomplete: a small strip of material exists between the edge of the visible strain field and the real edge of the sample (approximately shown by the black outline). For consistency, an analogous set of points is removed from the FEA set during processing.

Line scans of shear strains display a single peak within about 2 mm of the specimen midplane, followed by progressive decay with increasing distance (Figure 6). Strains from the elastic model are smaller than those from the inelastic model. The largest difference between predictions occurs at the peak, analogous to the open-hole case. For material M1, the predictions from the inelastic model fall at the bottom of the measured range, with the discrepancies increasing with increasing stress. For M2, the computed strains are consistently below the measurement values. At the fracture stress, the peak strains from the inelastic model are about half of the measured values.

For the *tensile strains*, the computed and measured fields and the corresponding line scans are similar to one another for both materials, and also are broadly analogous to the fields from open-hole tension. The strain fields show elevation ahead of the notch tips and nearly strain-free regions behind (Figure 7). The regions of elevated strain expand both along the loading direction and into the ligament as stress increases. The line scans show a single peak in strain magnitude at the notch tip and decay with distance (Figure 7). However, there are two notable differences between the measured and computed results. First, the peak measured strains at the fracture stress exceed those from the simulations, especially for material M2. Second, the measured strains furthest from the notch tip (near the free surface) fall below the computed values. In combination, these two features suggest that there is some degree of in-plane bending in the experiments. This discrepancy is examined in Section 3.6. The inability of the present simulations to capture the true boundary conditions introduces some degree of uncertainty in the assessment of the inelastic constitutive model. Regardless, the measurements show once again that the local tensile strains can exceed those obtained in unnotched tensile tests over distances of about 1-2 mm.

3.4. ***Edge-notched tension tests (a/W = 0.5)***

The macroscopic responses, measured and computed and for both materials, for edge-notched tension tests with this deeper notch are linear until 20 MPa for M1 and 15 MPa for M2 (Figures 3E and 3F), corresponding to 25% and 18% of the failure strengths. The stiffnesses of the computed responses agree with each other for each material but appear slightly larger than those of the measured responses in this regime. Higher stresses again produce progressively decreasing tangent moduli in the responses from the experiments and the inelastic model. The inelastic deformation is partially captured by the inelastic constitutive model (and not at all by the elastic model). The captured portion is less than that for the a/W = 0.3 edge notch. Displacements are thus underestimated by both models for both materials over essentially the entire loading. At fracture, the total displacements produced by the inelastic models are around 50% (M1) and 55% (M2) of the measured values, with the inelastic contributions being 10% and 30% of those computed total displacements.

The full-field strain distributions, measured and computed, contain the same features as those of the shallower notches: lobes of high shear strain (up to 0.005 for M1 and 0.007 for M2) emanate from the notch tips along the loading direction (Figure 8) while tensile strains are elevated directly ahead of the notch tip (Figure 9). Both expand with stress in the same manner as for the shorter edge notch. The shapes of these regions are also like those from the shallower notches, but discrepancies between the computed and measured strains are larger. The discrepancies are again larger for material M2 than for M1.

As follows from the similarity in the strain fields, the line scans are generally like those for the shallower notch as well, but with greater deviation of the predicted values from the measurements. The shear strains from the inelastic model are below the lower bound of the measured range beginning at low stresses for both materials (Figure 8). At the fracture stress, the peak shear strains predicted with the inelastic model are about one-quarter (M1) and one-third (M2) of the largest measured values. The tensile strains again suggest the occurrence of in-plane bending during the experiments. The peak tensile strains measured at the fracture stress exceed those from the simulations for both materials while the measured strains nearest the free surface are below the computed values, even becoming negative (Figure 9). Thus, there is again uncertainty in assessing the inelastic constitutive model for this loading condition; discrepancies cannot be conclusively assigned to differences in the situation modeled or to shortcomings of the inelastic constitutive model. However, as for the other loading conditions, the measurements show that the local tensile strains prior to rupture can exceed those obtained during unnotched tension over distances of 1-2 mm.

3.5. Edge-notched tension with uniform stress loading

In single-edge notched tension (SENT) tests, the loading axis is not aligned with the centerline of the net-section of the specimen. The misalignment of the external and internal forces induces moments and rotations in the material. At the ends of the specimens, these moments are resisted to varying extents based on the fixturing of the test. The FE models used in the preceding sections (and the appendices) of this thesis impose stress by applying a load at a single node and requiring that the displacements in the loading direction of all nodes along the width of that end of the specimen be equal. The forces required to cause those displacements are not constrained. This condition (hereafter, the uniform displacement Δ case) is one of two limiting idealizations. The other limit is one in which the stress along the width is uniformly distributed (hereafter, the uniform stress σ case). The former assumes that the load train is rigid such that the specimen cannot rotate. Achieving this experimentally requires a very stiff set of grips and clamping of a significant portion of the sample. The latter holds when there is no rotational stiffness to the sample motion, such as occurs for very long samples and pin loading[22].

The uniform displacement condition of the preceding simulations was chosen for two reasons. (i) The nature of the grips and the load train suggests a very high stiffness, especially in comparison to that of the test specimens. (ii) The crack mouth opening displacements (CMODs) in the elastic domain measured experimentally correlate more closely with those predicted using analytical solutions for the uniform displacement end condition[23] than those for the uniform stress condition[24] (Figure 10).

However, other evidence suggests that the uniform displacement condition is not maintained throughout the entirety of the experiment and that inelastic deformation is not the sole cause. As introduced in Sections 3.3 and 3.4, features in the line scans and tensile strain fields of the measured strains suggest in-plane bending during the experiments. Namely, the measured tensile strains exceed the values computed with the uniform-displacement model near the notch tip and fall below them near the free edge, becoming negative in some cases. These negative values in particular strongly suggest in-plane bending as they should not be possible for loading by uniform displacement of the ends. To further address this issue, rotations of initially horizontal lines midway between the notch plane and the gripped ends were computed from both the simulations and the measurements (Figure 11). The results show that, indeed, the amount of bending is more pronounced in the experiments than in the simulations. Evidently, despite the seemingly rigid grips and load train employed in the present experiments, sufficient compliance exists for significant bending to occur.

To further elucidate the effects of end conditions, simulations of SENT were conducted in which the applied stress was uniformly distributed across the width of the specimen while the associated displacements at those nodes were left unconstrainted. Otherwise, the sample geometries were identical to those of the previous simulations (Figure 12). Only the inelastic constitutive model was used for these simulations.

The macroscopic responses from the uniform stress simulations are initially linear. The stiffnesses of the computed responses in the linear regimes are less than those of the experiments and progressively decrease with stress (Figures 3C - 3F). The rates of the decrease are less than in the measurements, especially at stresses near the fracture stress. Thus, inelastic deformation is predicted by the model with this loading condition, but it does not develop at the same rate as in the experiments. Further, the predicted displacements for this end condition are *greater* than the measured values. At the fracture stress, the total displacements predicted with the uniform stress simulations exceed the measured totals by <10% of the measured total displacements for the shallower notches; those of the deeper notches exceed the measured values by >30%.

The full-field shear strains from these simulations (Figures 6 and 8) contain lobe features similar to those in the measured fields and from the other simulations. As in the prior simulations, these lobes grow parallel to the loading direction with increasing stress. For the a/W = 0.5 notches and at higher stresses for the a/W = 0.3 notches, there are secondary lobes of strain elevation ahead of the notch. There are hints of similar regions in some of the measured fields, but the strain magnitudes are near the level of the noise. No such regions are evident in the fields from the uniform displacement simulations. Discrepancies between the inelastic model and the measurements are greater for material M1 than for M2 for a/W = 0.3

but similar for a/W = 0.5. The primary lobes (those near the notch tip) qualitatively appear larger than those in the measured fields (except for a/W = 0.3 of M2) and those from the uniform displacement simulations.

Line scans of the shear strains (Figures 6 and 8) from this uniform stress case have similar shapes as those of the measurements and the other simulations, namely a single peak at a distance of about 2 mm from the notch tip followed by progressive decay with distance. The magnitudes at the peaks are greater than those of the previous simulations. For M1, the predicted magnitudes at the peaks exceed the measured values for both notch lengths. The degree of this overprediction diminishes with increasing stress. For M2, the predicted values for a/W = 0.3 exceed the measured values at low stresses but are within the measured range for higher stresses. For a/W = 0.5, the computed strains exceed the measured range for all stresses but, as for M1, the degree decreases with increasing stress.

The full-field tensile strains from these simulations are also similar to the measured fields (Figures 7 and 9). They contain a single, essentially elliptical, lobe emanating from the notch tip that grows radially with stress, and strain-free regions behind the notch tip. The lobes do not extend to the free edge, even at the higher stresses. Thus, the computed strains are not elevated at the free edge, unlike in the predictions from the uniform displacement simulations. At higher stresses, the lobes for a/W = 0.3 notches from the uniform stress simulations are qualitatively similar in size to those of the measurements; those from a/W = 0.5 notches are larger. The lobes are also larger than those of the uniform displacement simulations and show greater strain elevation near the notch tip.

Line scans of the tensile strains (Figures 7 and 9) from the uniform stress simulations are broadly of the same shape as those measured and those obtained from the other simulations; the strains peak at the notch tip and decrease with distance. At sufficiently low stresses, the computed strains for the uniform stress condition exceed the measured strains near the notch tip for both notch sizes. At higher stresses, the peak values predicted for the shallower notches are within the measured ranges while those for the deeper notches exceed the measured ranges. Near the notch tip, the measured strains decrease more rapidly than those of the uniform stress simulations. However, the decay of the measured strains slows near the center of the ligament while the computed strains continue to decrease. The computed strains near the free edge fall below the measured values and become negative for both notch lengths.

3.6. Fracture initiation

Based on the preceding measurements, observations, and computations, a rudimentary criterion for fracture initiation is proposed. Two features are deemed important. First, local strains at fracture exceed those obtained in standard tests without strain gradients. This condition persists over distances of 1-2 mm. (This length is large relative to both structural elements of the materials and the lengths used during data averaging.) Therefore, prediction based solely on peak values of strain (or stress) is inadequate. (This phenomenon has been broadly recognized in the ceramic- and polymer-matrix composite communities[1,2,18].) Second, the observed locations of fracture initiation in the open-hole tensile tests suggest that fracture is influenced by both the axial tensile strain and the shear strain. Qualitatively, this is evidenced by the observation that fracture initiates in locations where both strains are high. Based on these features, the proposed fracture criterion invokes a characteristic area over which the local conditions must meet the fracture criterion and combines the two strains (in a quadratic fashion analogous to stress-based criteria of Tsai-Wu[16] and Yamada-Sun[25] for polymer composites). The combined strain criterion is given by

$$\left(\frac{\varepsilon_{yy}^{i}}{\varepsilon_{yy}^{*}}\right)^{2}+\left(\frac{\gamma_{xy}^{i}}{\gamma_{xy}^{*}}\right)^{2}=1 \tag{5}$$

where ε_{yy}^{*} and γ_{xy}^{*} are the failure strains measured in uniaxial tension and pure shear, respectively, and ε_{yy}^{i} and γ_{xy}^{i} represent the local normal and shear strains. Fracture is assumed to occur when this condition is satisfied over a characteristic area, A_c, around the strain-concentrating feature.

A preliminary assessment of the proposed criterion was made by computing the spatial domains over which Eqn. 5 is satisfied at the onset of fracture. The domain boundaries for both materials and from both the measurements and the simulations are presented in Figure 13; the quantitative characteristic areas are given in Table 3. Because fracture is assumed to initiate at a single location, each connected region over which Eqn. 5 is satisfied is considered separately and the largest is taken as the characteristic area. Thus, for open-hole tension the areas of regions separated by the hole are not summed to calculate the characteristic area. For each of the materials the characteristic areas fall within narrow ranges across all specimen geometries. Assessment of the universality of this characteristic area would require additional tests on specimens containing holes of varying size and hence varying strain gradients. The areas from the predicted strains are smaller than those from the measured strains for all loading conditions.

Thus, strengths would be under-predicted for all conditions. For SENT the differences in boundary conditions (Section 3.5) likely contribute to the discrepancies.

4. Conclusions

1. Both oxide CMCs examined in this study exhibit nonlinear responses in open-hole and single edge-notched tensile tests. Macroscopic responses for open-hole tension are reproduced well by finite element simulations that employ the inelastic constitutive model but not (unsurprisingly) the elastic model.

2. Significant variations are obtained in measured strain fields around holes, presumably due to non-uniformities in composite microstructure. Nevertheless, strains computed using the non-linear constitutive model fall within the bounds of the experimental measurements over most of the loading history. Discrepancies in strain fields very near fracture may be attributed to two effects. First, there is likely some degree of strain softening in the most heavily strained regions: a feature that cannot be captured by a model predicated on monotonic loading. Second, the model assumes proportional loading throughout. Even before strain softening, proportionality may be lost and the fidelity of the predictions may become somewhat compromised.

3. Predicting the response of edge-notched tensile specimens is complicated by the apparent changes in boundary conditions during loading. Bending leads to strain elevations in the vicinity of the notch tip and strain reductions in regions distant from the notch tip. Thus, the uniform-displacement loading condition employed by the current FEA model is appropriate for the early portions of the loading histories, but begins to break down at higher stresses. At high stresses, the end condition instead begins to resemble a uniformly-distributed stress. However, such a condition is not fully attained even at the fracture stresses; therefore, the real end condition at these stresses is intermediate between those of the two limiting cases. Capturing these features would require analysis of the coupled

effects of the loading train stiffness and the notch-tip inelasticity in test specimens. Alternative experiments – based, for example, on center-notched tensile specimens – would probably provide a better assessment of the capabilities and limitations of the model.

4. The combination of the present finite element simulations and the experimental measurements provide insights into the local conditions for fracture initiation. Notably, both normal and shear strains play roles in the process. Additionally, there appears to be a critical size scale associated with the heavily-strained material at the point at which fracture initiates. The proposed fracture criterion – based on attainment of a critical combination of normal and shear strains over a characteristic area – contains the essential ingredients, although its predictive capability has yet to be critically assessed.

References

1. McNulty, J. C., Zok, F. W., Genin, G. M. & Evans, A. G. Notch-Sensitivity of Fiber-Reinforced Ceramic-Matrix Composites: Effects of Inelastic Straining and Volume-Dependent Strength. *J. Am. Ceram. Soc* **82,** 1217–1245 (1999).
2. Heathcote, J. a, Gong, X., Yang, J. Y., Ramamurty, U. & Zok, F. W. In-Plane Mechanical Properties of an All-Oxide Ceramic Composite. *J. Am. Ceram. Soc.* **82,** 2721–2730 (1999).
3. Rajan, V. P., Shaw, J. H., Rossol, M. N. & Zok, F. W. An elastic-plastic constitutive model for ceramic composite laminates. *Compos. Part A Appl. Sci. Manuf.* **66,** 44–57 (2014).
4. Bheemreddy, V., Chandrashekhara, K., Dharani, L. R. & Hilmas, G. E. Computational study of micromechanical damage behavior in continuous fiber-reinforced ceramic composites. *J. Mater. Sci.* **51,** 8610–8624 (2016).
5. Camus, G. Modelling of the mechanical behavior and damage processes of fibrous ceramic matrix composites: Application to a 2-D SiC/SiC. *Int. J. Solids Struct.* **37,** 919–942 (2000).
6. Pineda, E. J., Waas, A. M., Bednarcyk, B. A., Collier, C. S. & Yarrington, P. W. Progressive damage and failure modeling in notched laminated fiber reinforced composites. *Int. J. Fract.* **158,** 125–143 (2009).
7. Zhang, D., Meyer, P. & Waas, A. M. An experimentally validated computational model for progressive damage analysis of notched oxide/oxide woven ceramic matrix composites. *Compos. Struct.* **161,** 264–274 (2017).
8. Tushtev, K., Horvath, J., Koch, D. & Grathwohl, G. Deformation and failure modeling of fiber reinforced ceramics with porous matrix. *Adv. Eng. Mater.* **6,** 664–669 (2004).
9. Budiansky, B., Hutchinson, J. W. & Evans, A. G. Matrix Fracture in Fiber-Reinforced Ceramics. *J. Mech. Phys. Solids* **34,** 167–189 (1986).
10. Marshall, D. B. THE MECHANICS OF MATRlX CRACKING BRITTLE-MATRIX FIBER COMPOSITES. **33,** 2013–2021 (2013).
11. Hutchinson, J. W. & Jensen, H. M. MODELS OF FIBER DEBONDING AND PULLOUT IN BRITTLE COMPOSITES WITH FRICTION. *Mech. Mater.* **9,** 139–163 (1990).
12. Rajan, V. P. & Zok, F. W. Effects of non-uniform strains on tensile fracture of fiber-reinforced ceramic composites. *J. Mech. Phys. Solids* **60,** 2003–2018 (2012).
13. Aveston, J., Cooper, G. A. & Kelly, A. Single and multiple fracture: the properties of fiber composites. *Prop. fibre Compos.* 2019 (1971).
14. Beyerle, D. S., Spearing, S. M. & Evans, A. G. Damage Mechanisms and the Mechanical Properties of a Laminated 0/90 Ceramic/Matrix Composite. *J. Am. Ceram. Soc.* **75,** 3321–3330 (1992).
15. Tsai, S. W. *Strength characteristics of composite materials. NASA Contractor Report (NASA CR-224).* (1965).
16. Tsai, S. W. & Wu, E. M. A General Theory of Strength for Anisotropic Materials. *J. Compos. Mater.* **5,** 58–80 (1971).
17. Rajan, V. P. & Zok, F. W. Stress distributions in bluntly-notched ceramic composite laminates. *Compos. Part A Appl. Sci. Manuf.* **60,** 15–23 (2014).
18. Whitney, J. M. & Nuismer, R. J. Stress Fracture Criteria for Laminated Composites Containing Stress Concentrations. *J. Compos. Mater.* **8,** 253–265 (1974).
19. Mattoni, M. A. & Zok, F. W. Strength and notch sensitivity of porous-matrix oxide composites. *J. Am. Ceram. Soc.* **88,** 1504–1513 (2005).
20. Zok, F. W. Developments in oxide fiber composites. *J. Am. Ceram. Soc.* **89,** 3309–3324 (2006).
21. Tankasala, H. C., Deshpande, V. S. & Fleck, N. A. Notch sensitivity of orthotropic solids: interaction of tensile and shear damage zones. *Int. J. Fract.* **212,** 123–142 (2018).
22. Journal, I. & Publishers, K. A. A method for determing the stress intensity factor of a single edge notched tensile specimen. *Int. J. Fract.* 3–8 (2003).
23. John, R. & Rigling, B. Effect of height to width ratio on K and CMOD solutions for a single edge cracked geometry with clamped ends. *Eng. Fract. Mech.* **60,** 147–156 (1998).
24. Tada, H., Paris, P. C. & Irwin, G. R. *The stress analysis of cracks handbook*. *New York: ASME Press* **1,** (2000).
25. Yamada, S. E. & Sun, C. T. Analysis of Laminate Strength and Its Distribution. *J. Compos. Mater.* **12,** 275–284 (1978).

Table 1. Calibration constants used in the inelastic model.

Material	C_o	C_s	C_{45}
M1	1	3.59	2.50
M2	1	5.41	3.67

Table 2. Elastic constants measured for oxide CMCs M1 and M2.

Material	E_0 (GPa)	E_{45} (GPa)	ν_0	G_{xy} (GPa)	ν_{45}
M1	94.0	56.4	0.02	18.7	0.50
M2	67.8	50.5	0.04	21.8	0.30

Table 3. Areas (mm^2) over which Eqn. 5 is satisfied for all loading conditions for oxide CMCs M1 and M2 using measured (*DIC*) and computed (*FEA*) strain fields.

	M1		M2	
	DIC	FEA	DIC	FEA
OHT	13.8	5.1	16.4	11.0
	6.1		14.2	
	14.2		–	–
SENT a/W = 0.3	10.0	0.8	15.1	3.8
	6.5		14.1	
	6.3		–	–
SENT a/W = 0.5	8.8	N/A	19.8	7.2
	7.7		15.9	

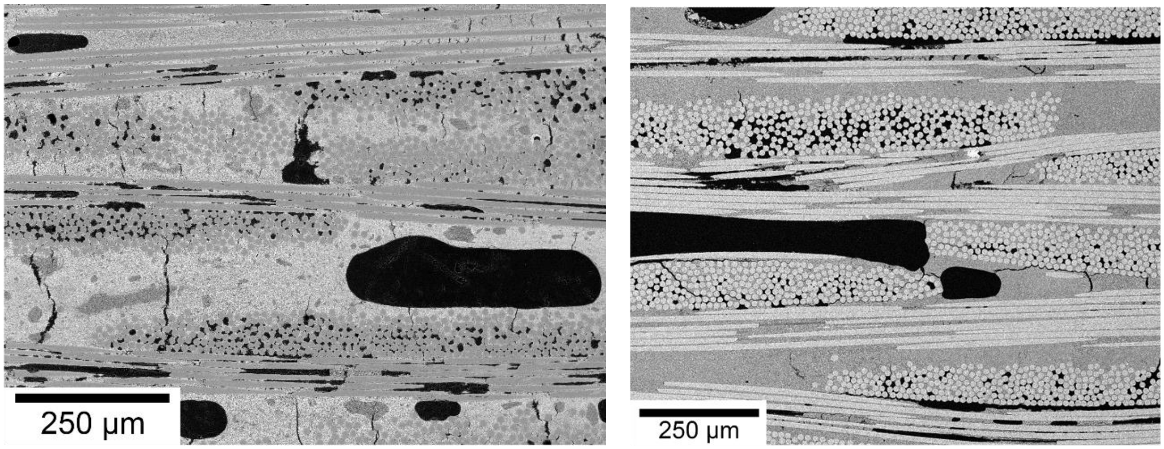

Figure 1. Backscatter SEM micrographs of polished cross-sections through samples of as-manufactured material M1 (left) and material M2 (right).

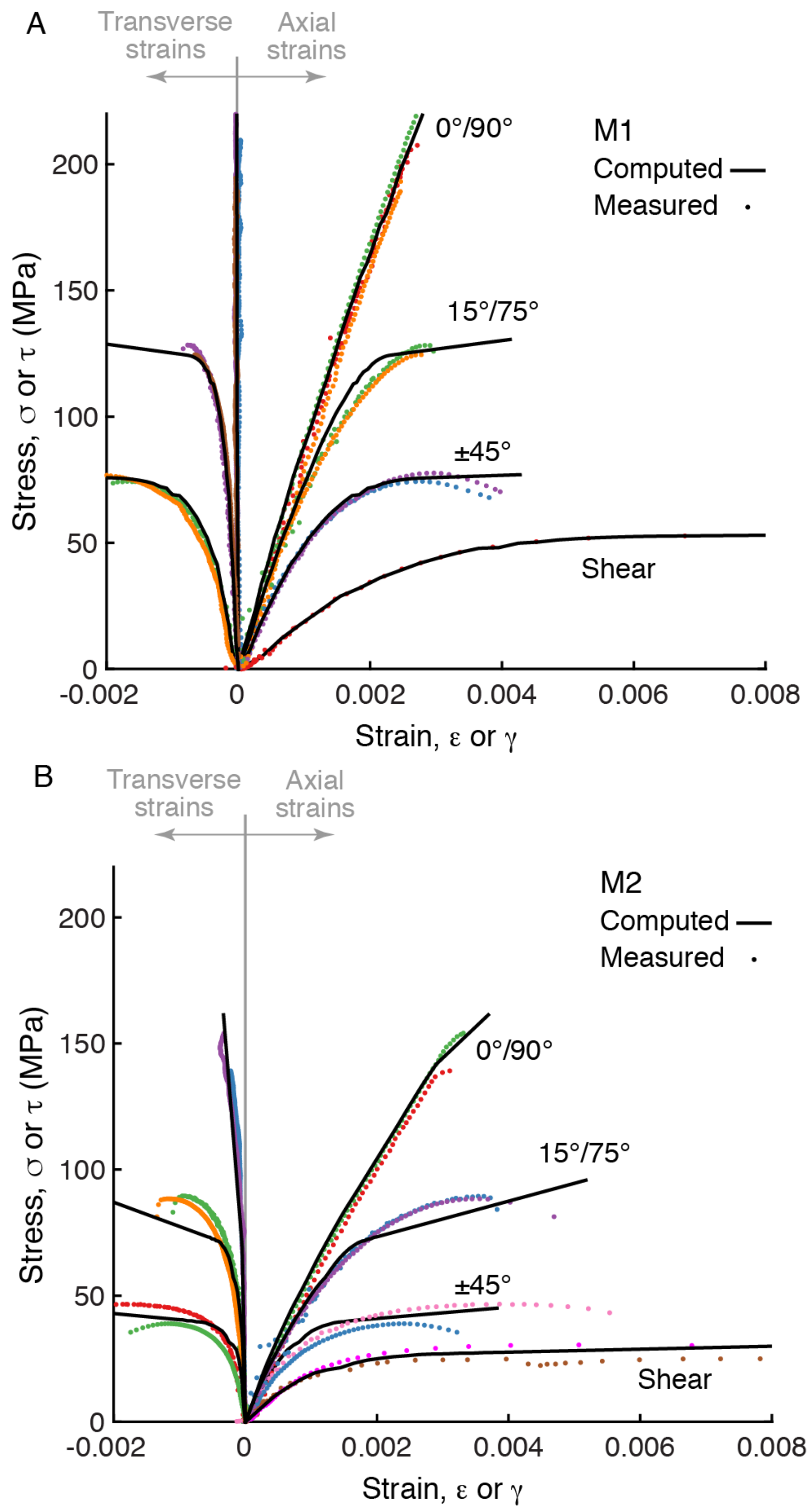

Figure 2. Measured and computed axial and transverse stress-strain curves for (A) material M1 and (B) material M2. Computed curves for 0°/90°, ±45°, and shear are averages through the hardening regime and then extrapolated at a constant tangent modulus; those for 15°/75° are from Equation 4. The agreement illustrates that the model is adequately calibrated, and that the expected stress-strain relationships hold for these materials.

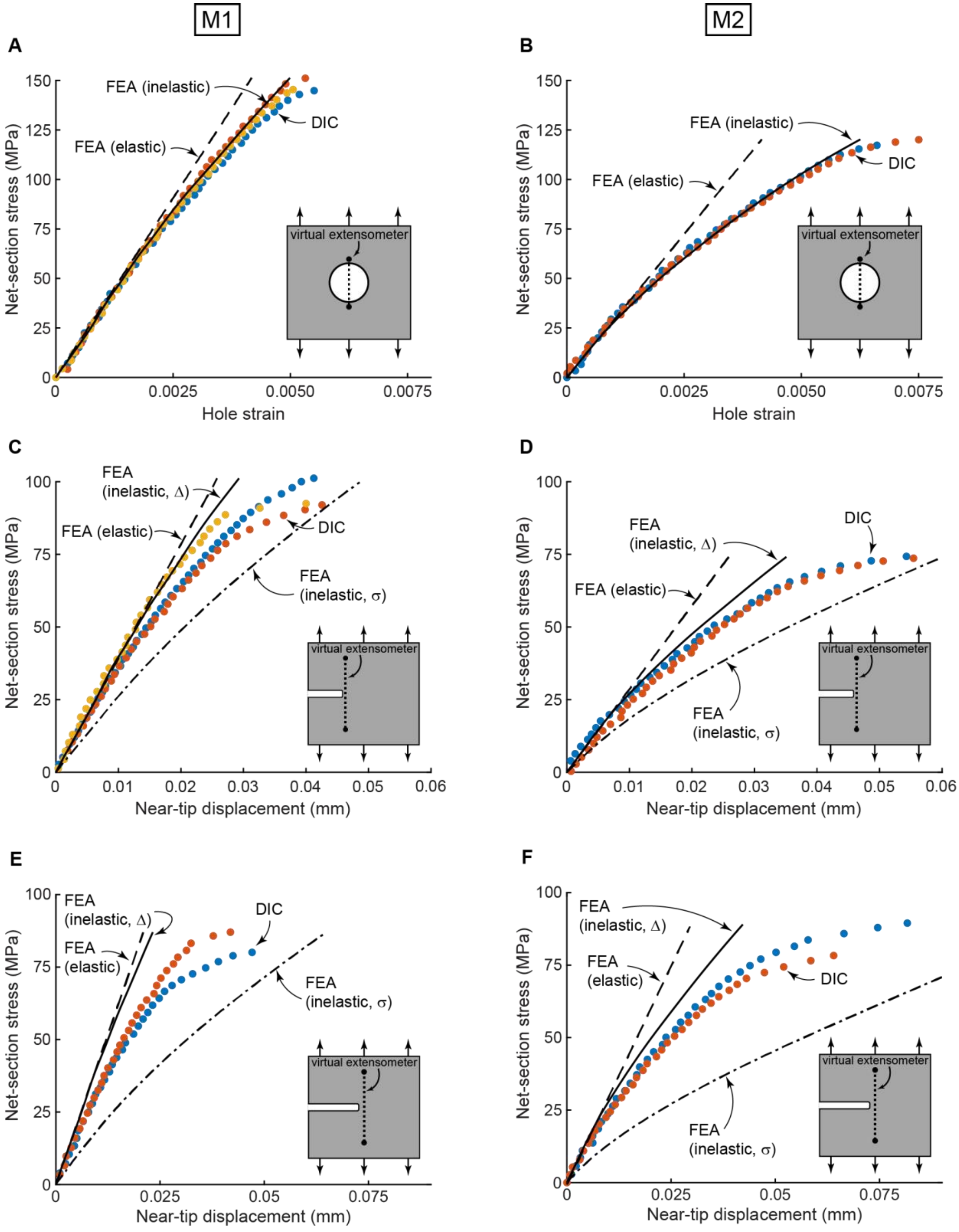

Figure 3. Measured and predicted global responses for open-hole tension and edge-notched tension of material M1 (A, C, and E) and M2 (B, D, and F). Hole strain is the strain of an extensometer that spans the hole along the centerline of the sample. Near-tip displacement is the change in length of an extensometer just in front of the edge notches.

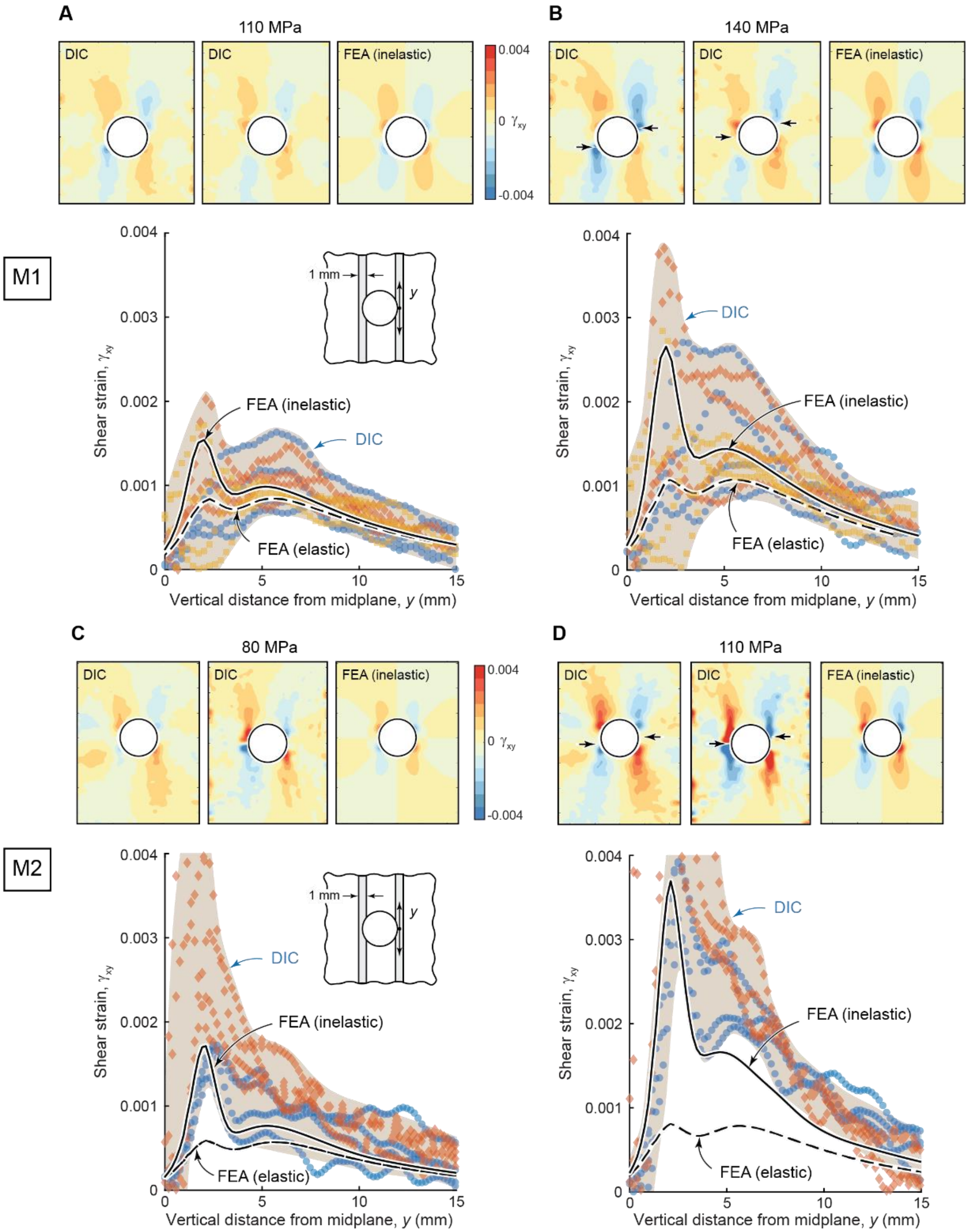

Figure 4. Comparisons of measured and computed shear strains for open-hole tension at two representative stresses for material M1 (A, B) and M2 (C, D). Full-field strains are shown for the experiments and FEA with the inelastic model; the plots additionally include results from line scans from the elastic model. The shaded bands in the plots from the line scans indicate the approximate range of experimental values. Different colors and symbols in the line scans from DIC measurements indicate different samples. Arrows in the full-field strain maps of B and D indicate the locations of future cracks which cause fracture.

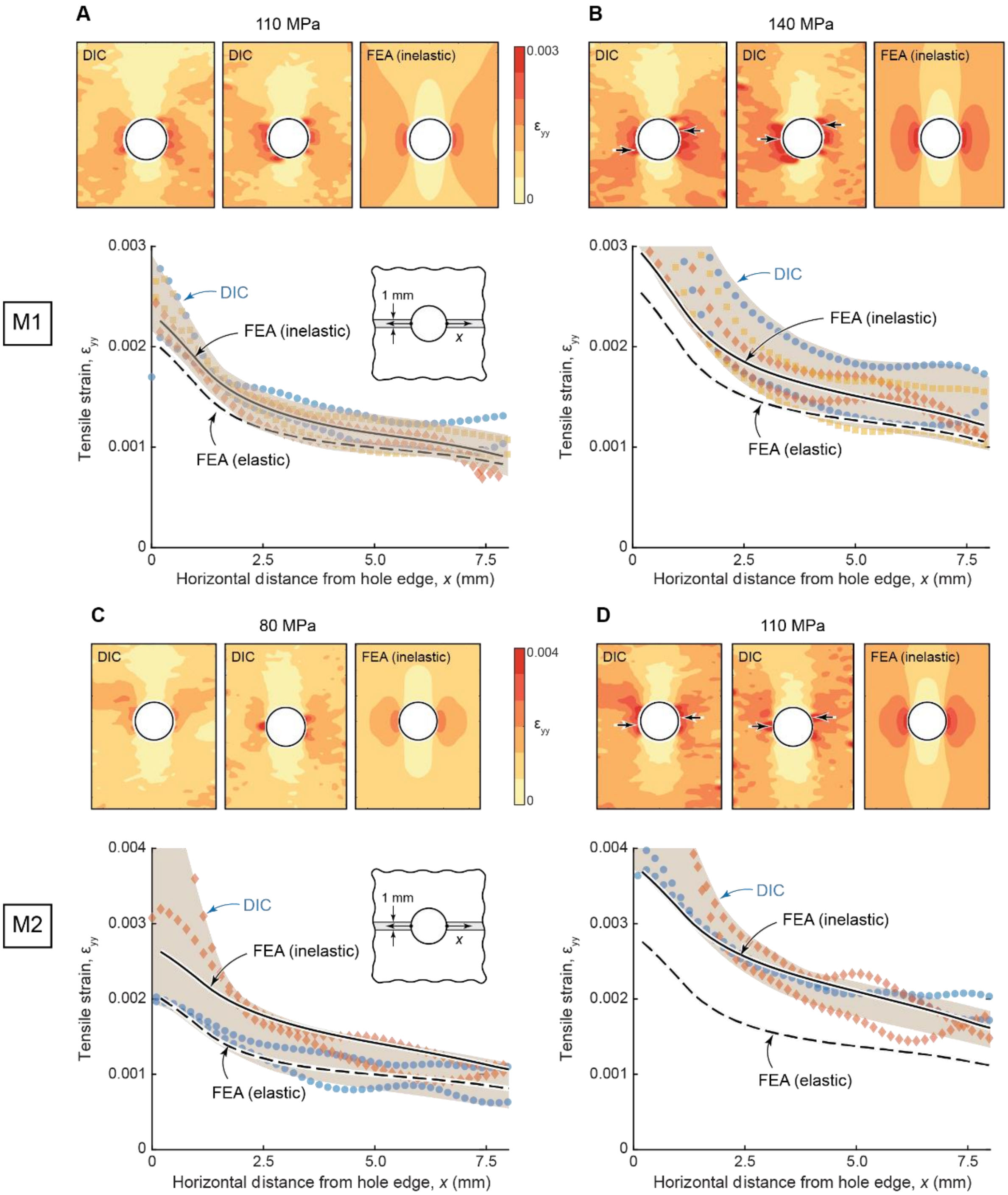

Figure 5. Comparisons of measured and computed tensile strains for open-hole tension at two representative stresses for material M1 (A, B) and M2 (C, D), analogous to the prior figure.

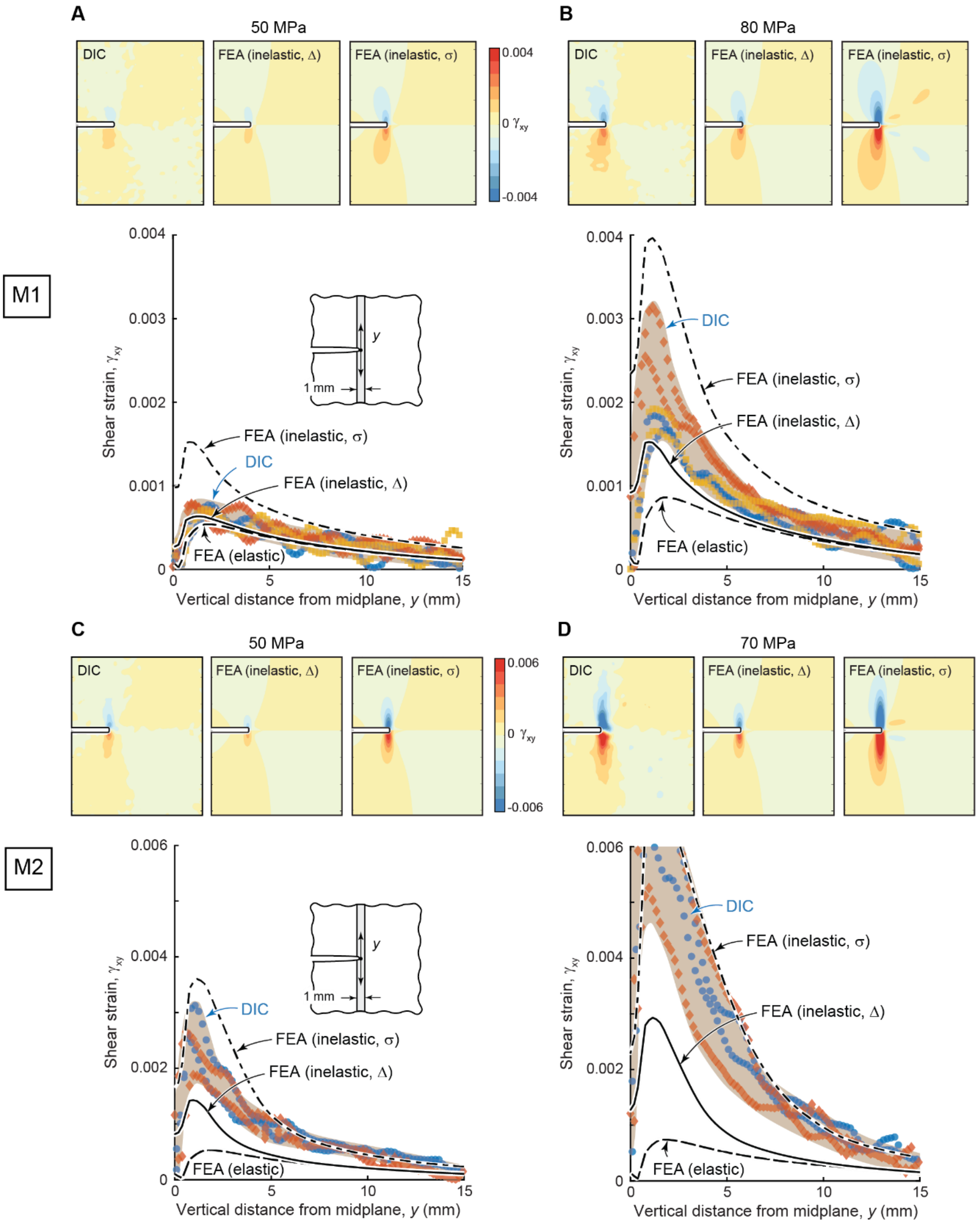

Figure 6. Comparisons of measured and computed shear strains for edge-notched tension with notch length/gauge-width ratio of a/W = 0.3 at two representative stresses for material M1 (A, B) and M2 (C, D). Note that predictions via FEA with the inelastic model for both the uniform displacement Δ and uniform stress σ cases are included.

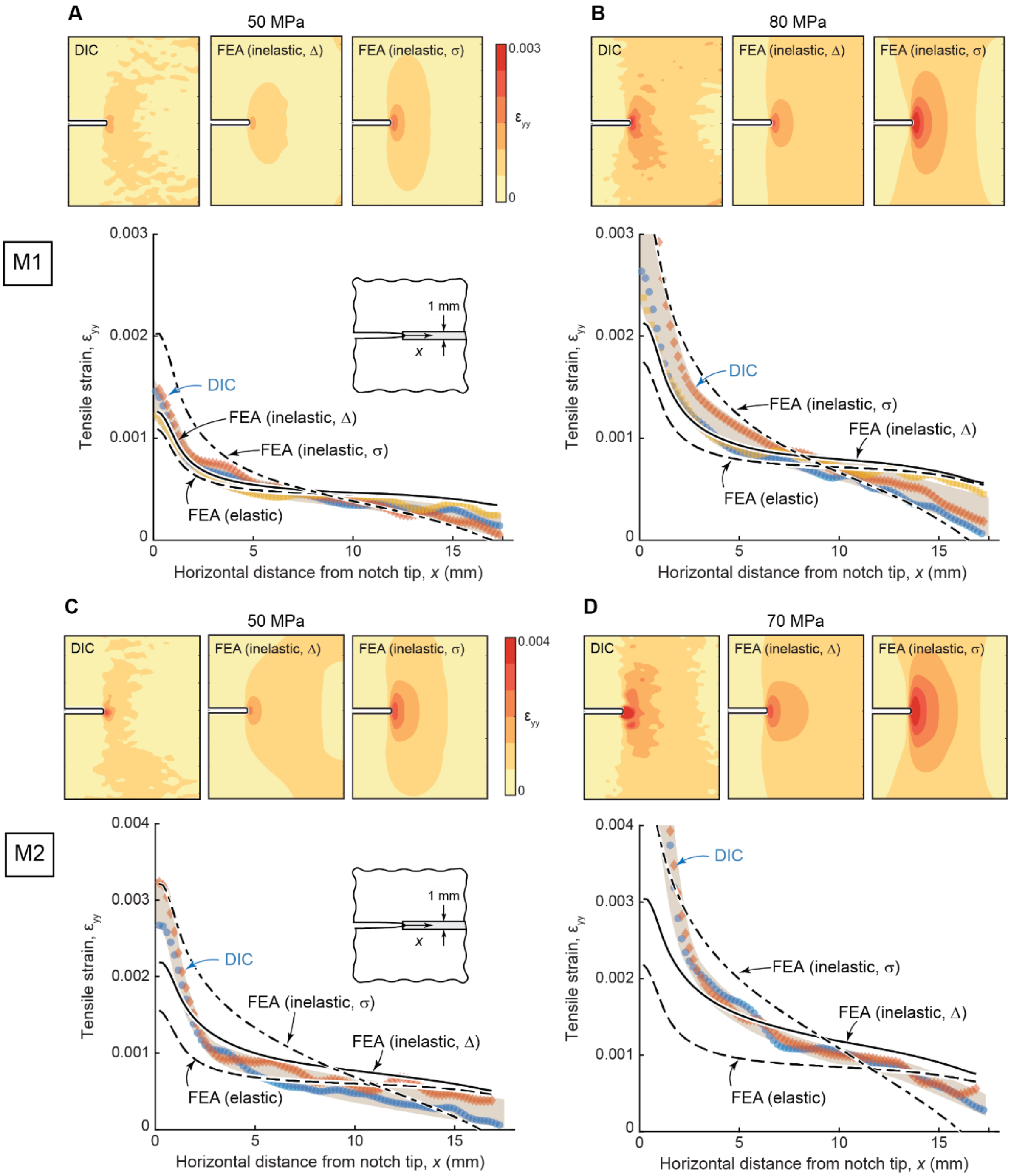

Figure 7. Comparisons of measured and computed tensile strains for edge-notched tension with notch length/gauge-width ratio of a/W = 0.3 at two representative stresses for material M1 (A, B) and M2 (C, D).

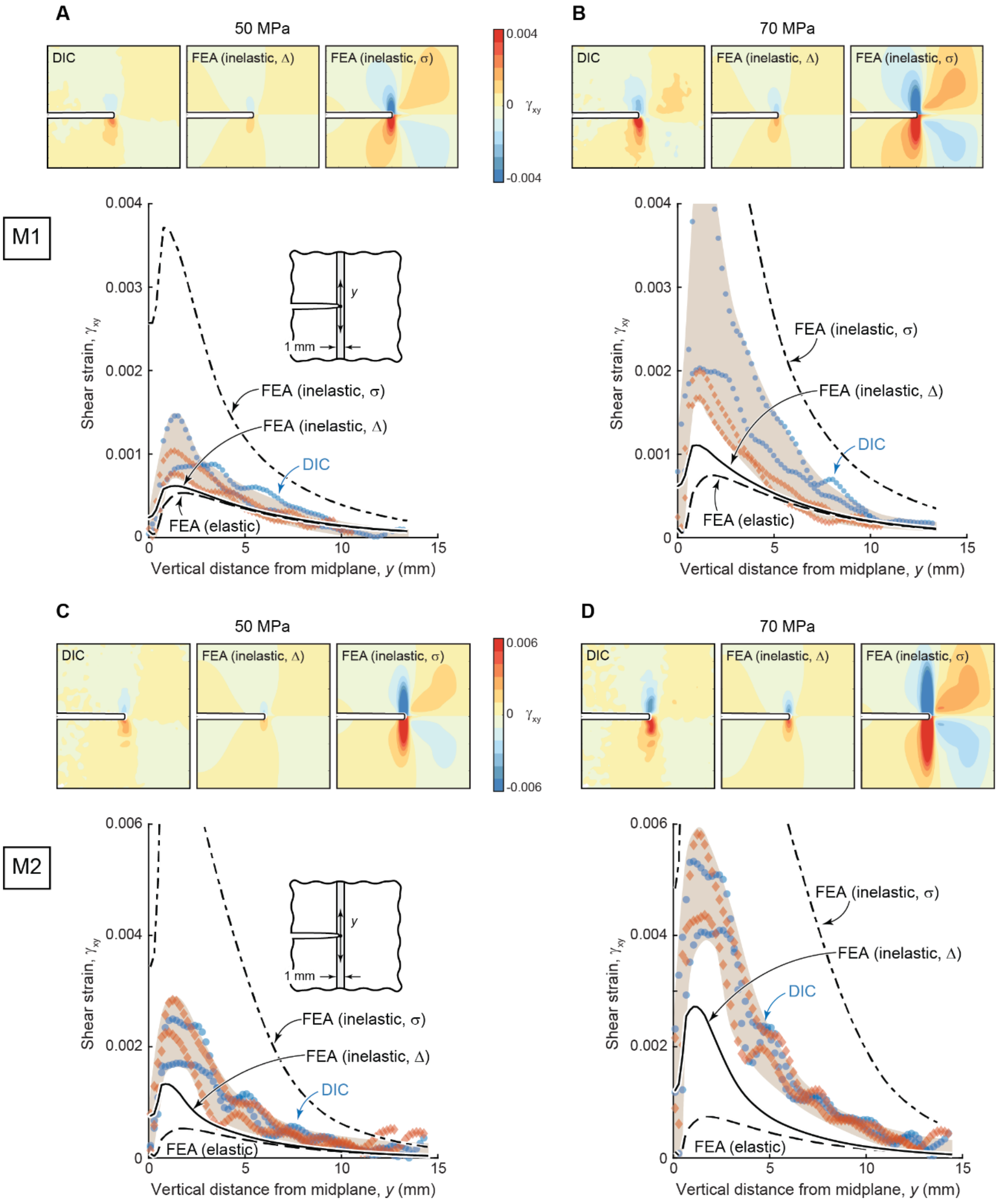

Figure 8. Comparisons of measured and computed shear strains for edge-notched tension with notch/gauge width ratio of a/W = 0.5 for material M1 (A, B) and M2 (C, D).

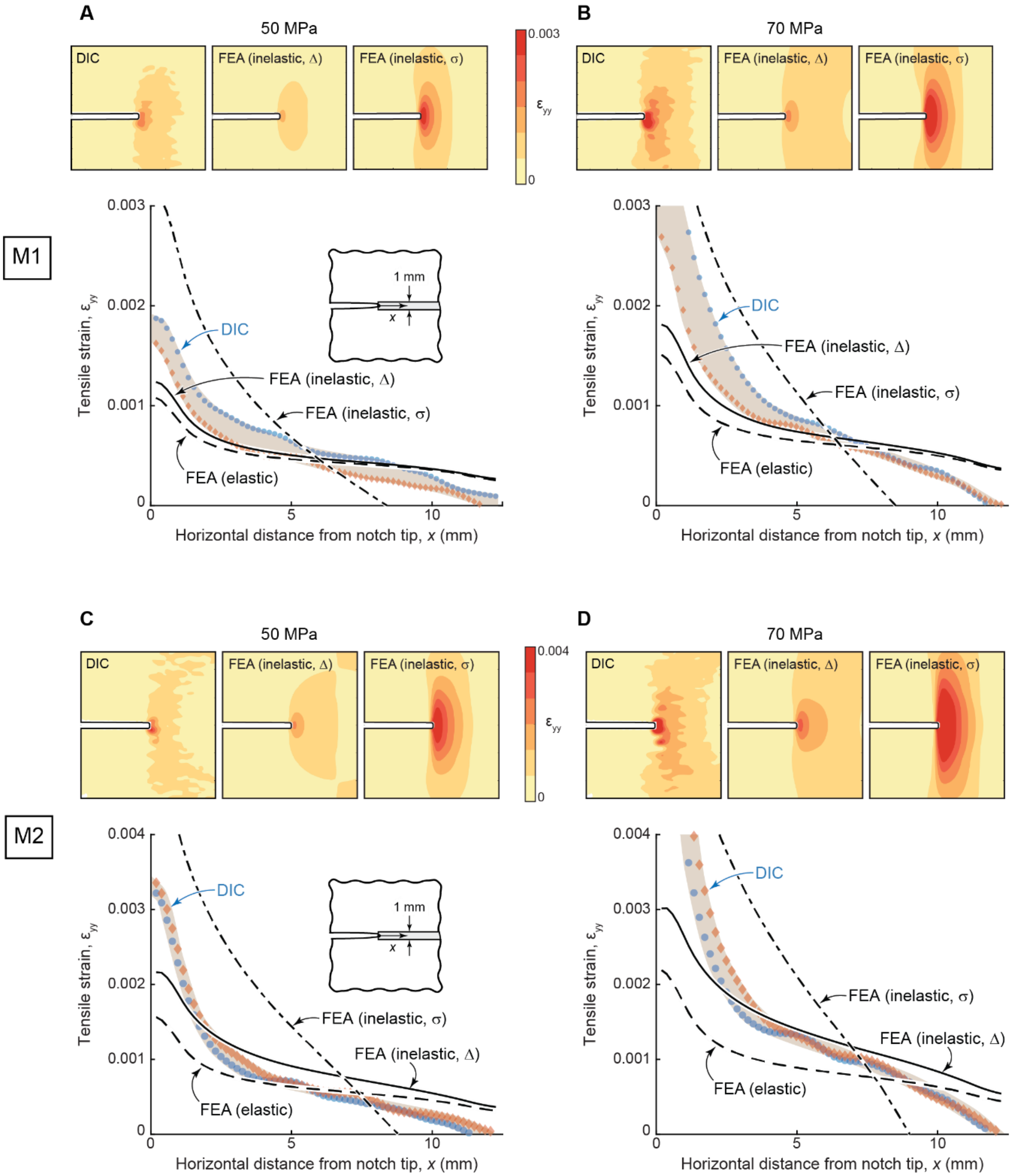

Figure 9. Comparisons of measured and computed tensile strains for edge-notched tension with notch/gauge width ratio of a/W = 0.5 for material M1 (A, B) and M2 (C, D).

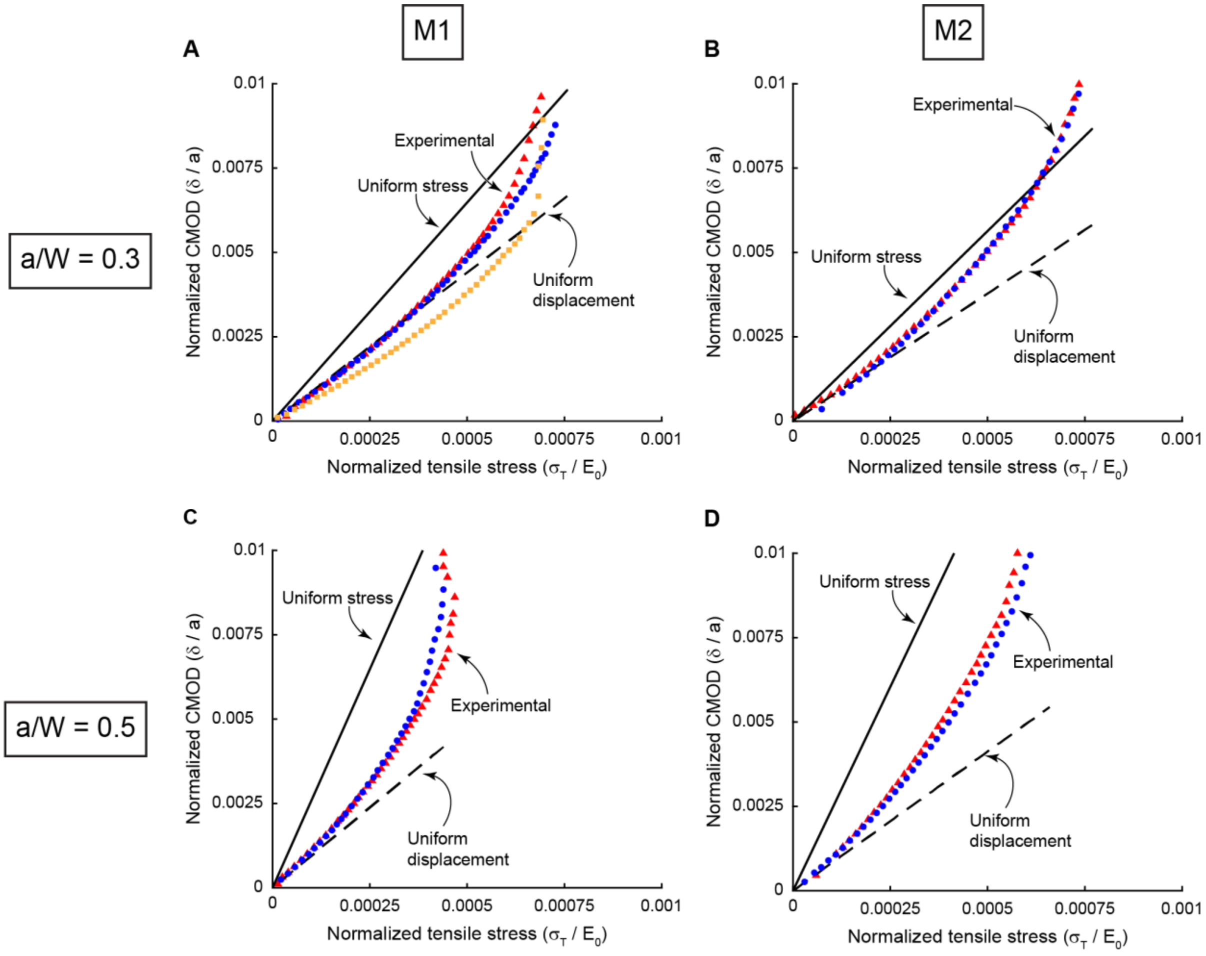

Figure 10. At low stresses, measured crack mouth openings from the SENT tests more closely match the analytical solution which assumes that displacement is uniform across the gripped ends of the specimens. Higher stresses produce a shift away from this limiting case. A and C are for material M1 with notch/gauge width ratios of a/W = 0.3 and 0.5; B and D are for material M2.

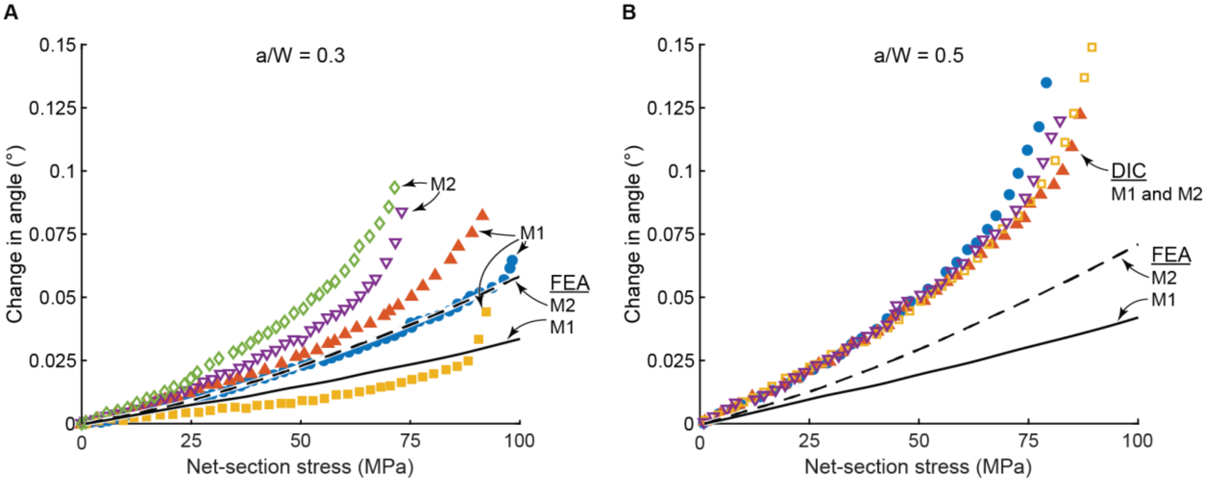

Figure 11. The rotation of SENT samples during experiments is larger than that of the simulations, indicating non-negligible compliance in the load train.

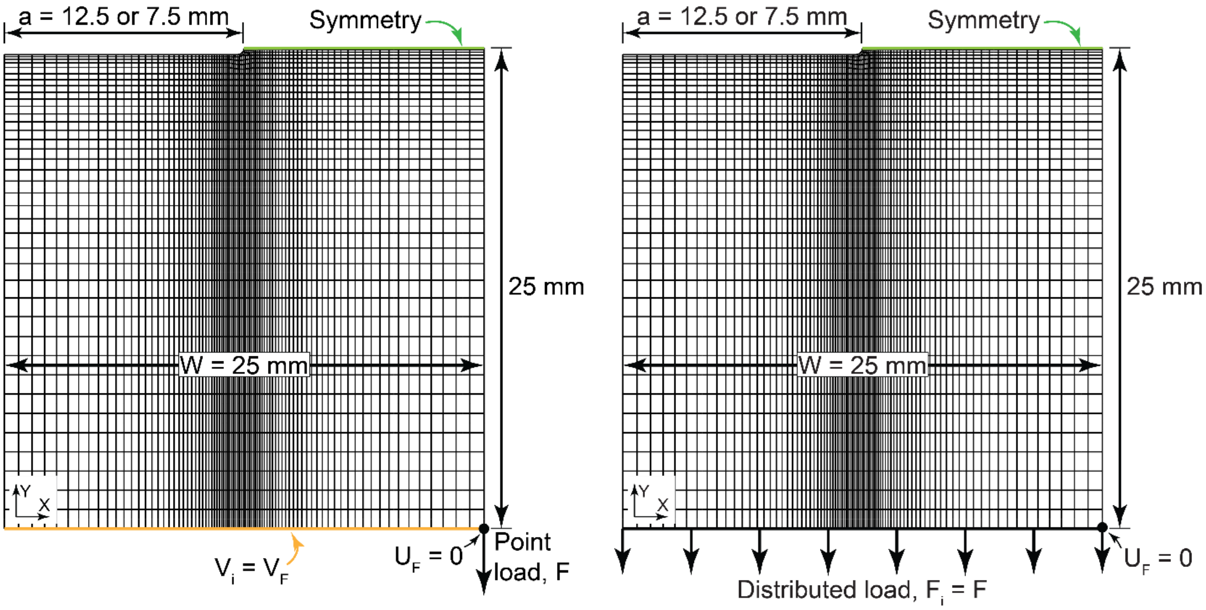

Figure 12. FE model geometry and boundary conditions for simulations with stress (left) and displacement (right) distributed uniformly across the end of the specimen.

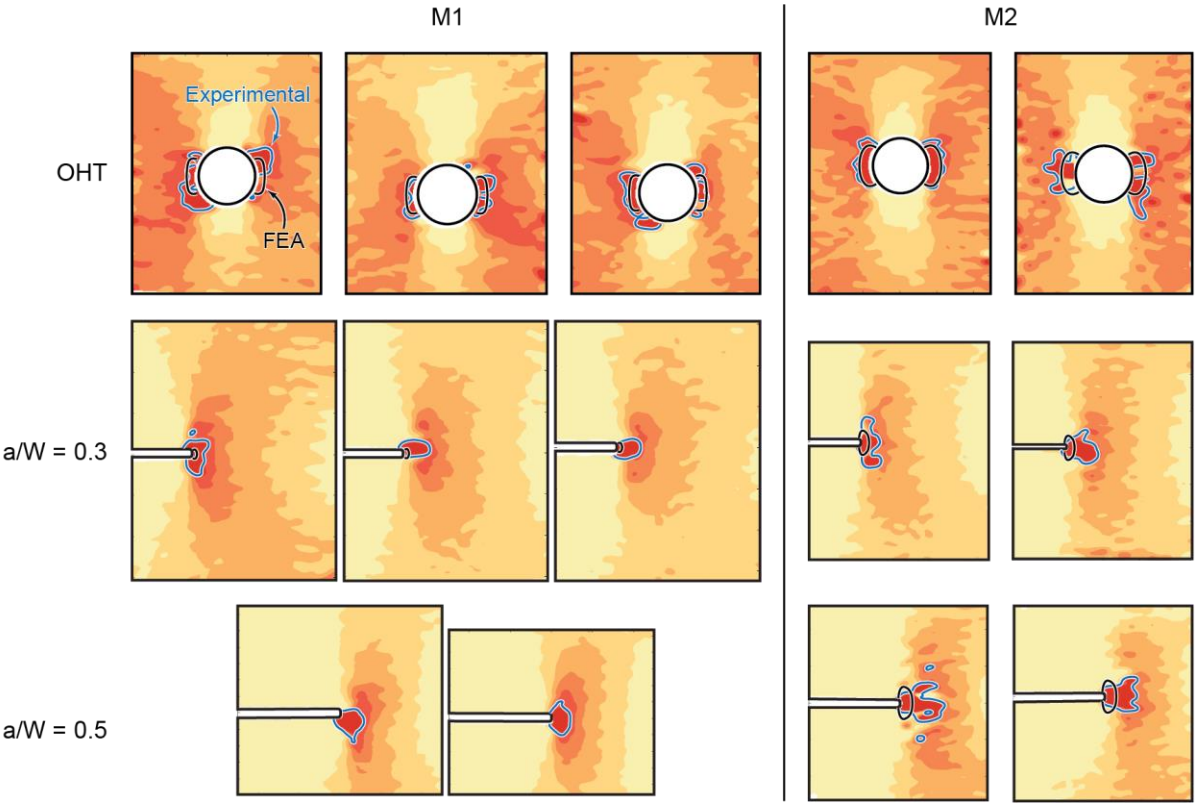

Figure 13. Boundaries over which the combined strain criterion (Eqn. 5) is satisfied at the failure stress evaluated using experimental strains (blue) and strains from the inelastic model (black). For material M1 there are no contours from the inelastic model for the a/W = 0.5 notch.

Appendix A: Refinement to calibration of the constitutive model

Determination of the constants C_{45} and C_s of the inelastic constitutive model was initially based on experimental measurements from three tests: 0°/90° tension, ±45° tension, and 0°/90° shear. Specifically, the two constants were first estimated from the 0°/90° tension and 0°/90° shear tests; then the fidelity of the model predictions was assessed by comparing predicted and measured responses for a ±45° tension test. During the course of this study, it was recognized that the procedures for determining and assessing the coefficients were, in many cases, unreliable. That is, satisfactory fits could be obtained for these three specific test types but not for others. Consequently, an additional set of test data – from 15°/75° tension tests – was incorporated into the procedure. The origins of the problem and the mitigation strategy follow.

The nature of the problem emerges from inspection of the form of the predicted response for ±45° tension. Rearranging Eqns. 21 and 22 of the original formulation of the model[3], the predicted longitudinal strain $\varepsilon_{45}(\sigma)$ of ±45° tension is found to be:

$$\varepsilon_{45}(\sigma) = \frac{C_0}{2C_{45}}\left[\varepsilon_0\left(\frac{C_{45}\sigma}{C_0}\right) + \epsilon_{0T}\left(\frac{C_{45}\sigma}{C_0}\right)\right] + \frac{C_s}{4C_{45}}\gamma_s\left(\frac{C_{45}\sigma}{C_s}\right), \tag{A1}$$

where ε_0 and ε_{0T} are measured strains as functions of stress σ in the axial and transverse directions from 0°/90° tension; γ_s is the measured strain from Iosipescu shear; and C_0, C_{45}, and C_s are the calibration constants (C_0 being taken to be unity). The dominant contribution to $\varepsilon_{45}(\sigma)$ is the last term on the right side of (Eqn. A1): the strain γ_s from the shear test. But this term is affected only by the *ratio* C_s/C_{45}, not by the individual values of *these constants*.

Furthermore, not only are the contributions from the two terms within […] small, the two are comparable in magnitude and of opposite sign. The net result is that seemingly successful validation of the model can be obtained using a wide range of values of C_s and C_{45}, subject only to the constraint that their ratio remains constant.

The problem can also be readily demonstrated through the following parametric study. Here the predicted ±45° tensile response was computed for three ratios of C_s/C_{45} for each material while the individual values were varied. One ratio was that found using the original calibration method; the individual values were increased and decreased by factors of 2. The other ratios were $C_s/C_{45} = 2$ and $C_s/C_{45} = 1$ (the former being a physical limit on the ratio and the latter chosen for reasons of numerical stability). For each of these one of the calibration constants was held at the value of the original calibration while the other was adjusted to reach the stated ratio. (The required increases/decreases were ~50% of the original values.) As shown in Figure A1, changes to the ratios shift the plateaus of the computed curves by factors of about 2, but changes made to C_s and C_{45} cause shifts of only about 1%.

The effects of the inferred calibration constants become evident when the parametric studies described above are repeated for the 15°/75° tension test. The predicted axial strain for this orientation ε_A is given by Eqn. 4 from Section 2.4:

$$\varepsilon_A(\sigma) = \frac{C_0}{8\,\overline{C}}\left[7\varepsilon_0\left(\frac{\overline{C}}{C_0}\sigma\right) + \varepsilon_{0T}\left(\frac{\overline{C}}{C_0}\sigma\right)\right] + \frac{C_s}{16\overline{C}}\gamma_s\left(\frac{\overline{C}}{C_s}\sigma\right); \qquad \overline{C} = \frac{1}{2}\sqrt{3C_0^2 + C_{45}^2} \tag{4}$$

The results are shown in Figure A2. In this case, the predictions are sensitive to both the ratio *and* the individual values of C_s and C_{45}. The degree of hardening increases with C_s/C_{45} ratio (as for the ±45° test), and, for a given ratio, increases with magnitude of the constants. Note also that for both materials the best agreement between computed and measured responses is obtained for a combination of C_s and C_{45} different from that found via the original calibration procedure. To mediate the problem, fitting to the test data from 15°/75° tension was incorporated into calibration, resulting in the procedure described in Section 2.4.

The key conclusion is that the three data sets initially proposed for model calibration and validation[3] do not accurately define the constitutive model. The addition of the 15°/75° tension test significantly improves the accuracy of the calibration constants and the fidelity of the model predictions.

Table A1. Calibration constants for the parametric study of material M1.

	Best-fit (±45°)	Ratio = same, values / 2	Ratio = same, values × 2	Ratio → 2, C_{45} ↓	Ratio → 2, C_s ↑	Ratio → 1, C_{45} ↑	Ratio → 1, C_s ↓
C_s	1.88	0.94	3.75	1.88	2.61	1.88	1.31
C_{45}	1.31	0.65	2.61	0.94	1.31	1.88	1.31
C_s/C_{45}	1.44	1.44	1.44	1.99	1.99	1	1

Table A2. Calibration constants for the parametric study of material M2.

	Best-fit (±45°)	Ratio = same, values / 2	Ratio = same, values × 2	Ratio → 2, C_{45} ↓	Ratio → 2, C_s ↑	Ratio → 1, C_{45} ↑	Ratio → 1, C_s ↓
C_s	3.69	1.84	7.37	3.69	5.01	3.69	2.50
C_{45}	2.50	1.25	5.01	1.84	2.50	3.69	2.50
C_s/C_{45}	1.47	1.47	1.47	1.99	1.99	1	1

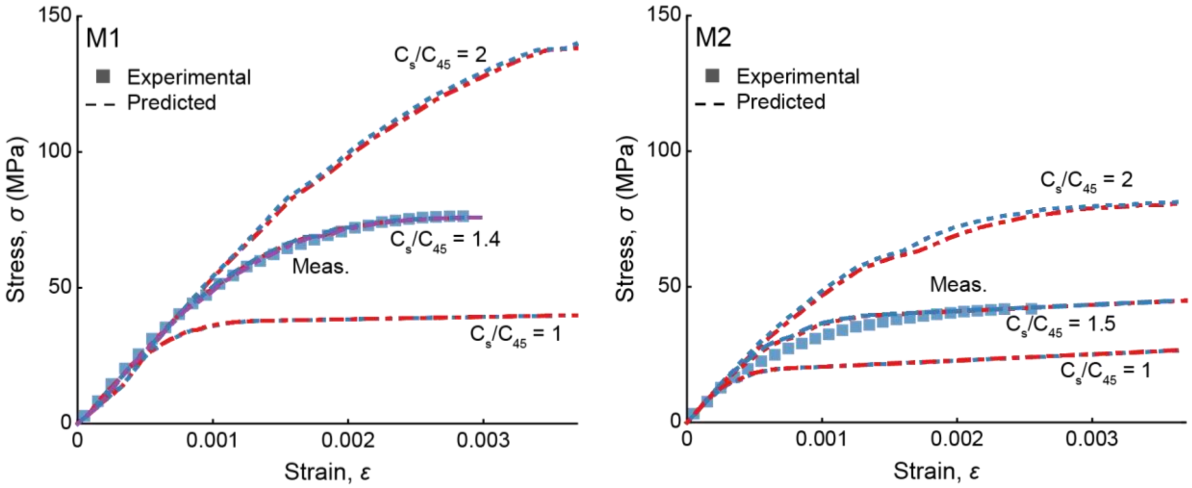

Figure A1. The response predicted for ±45° uniform tension changes with the ratio of C_s/C_{45}, but not as the magnitudes of C_s and C_{45} are varied at a constant ratio.

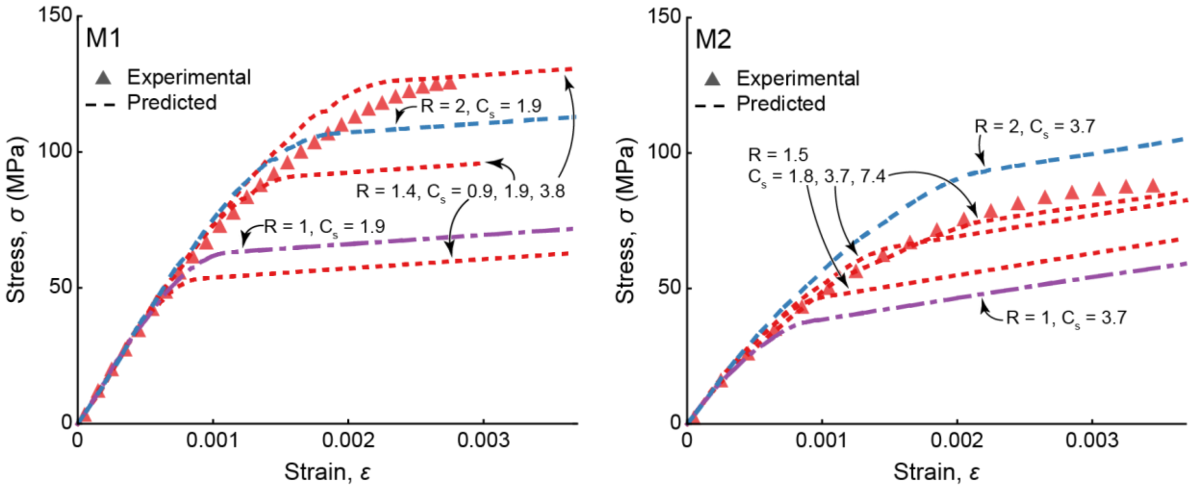

Figure A2. The behavior predicted for 15°/75° uniform tension changes with both *R*, the ratio of C_s/C_{45}, and the magnitudes of C_s and C_{45} for a constant *R*. For clarity, only a single line for $R = 1$ and $R = 2$ are shown. These lines are those for which C_s is the value found during calibration. Variation with C_s like that for the intermediate *R* values occurs for these ratios as well.

Appendix B: Effects of terminal tangent modulus on strain predictions

A tacit assumption in the implementation of the inelastic constitutive law is that, for stresses exceeding the maximum values obtained in the calibration tests, the calibration curves can be linearly extrapolated to higher values using a tangent modulus defined by the last two data points in the corresponding stress-strain curve. This assumption is expected to be reasonable when the volume of material experiencing an "overload" is small and the overload itself is small relative to the ultimate strength. But this assumption is almost certainly unconservative; locally, the tangent modulus is expected to progressively decrease as the failure point is approached. One method to incorporate these effects is to prescribe a reduced tangent modulus in the post-maximum domain. (Invoking strain *softening* is not an option with the present constitutive model because of the underlying assumption of *monotonic* proportional loading.)

To assess the potential effects of reduced hardening at the highest stresses on the predicted strain distributions in the notched and open hole specimens, additional FEA simulations were performed assuming that the terminal tangent modulus is reduced by a factor of 5 relative to that calculated with the last two experimentally-measured data points, as illustrated in Figure B1. The predicted macroscopic responses from these simulations are plotted on Figure B2. Here the initial moduli and onset of nonlinearity are essentially unchanged for both materials. In the inelastic regimes, the predicted hole strains and near-tip displacements from the new simulations are larger than those from the previous simulations, the effects being more pronounced in material M2. For the OHT tests, the hole strains in M1 remain within the range of the measurements for the entire loading, albeit closer to the top of the experimentally-measured range. For material M2, the predicted hole strains overestimate the measured values at stresses exceeding about 50% of ultimate; at the fracture stress, the predicted hole strains are about 20% greater than the measured values. For SENT tests, the computed near-tip displacements are also elevated, bring the predictions into better agreement with the measured values.

The computed strain fields from both sets of simulations show similar qualitative features (Figures B3 - B8). For material M1, the new simulations consistently bring the predictions closer to the experimental data. But the new simulations for material M2 appear to produce larger changes, often exacerbating the differences with the measured values. The origins of the latter trends are presently not understood.

Although the new simulations (with the reduced terminal tangent moduli) are based on rather ad hoc assumptions about the constitutive response near ultimate failure, they do show that the predictions are indeed sensitive to the responses in this domain. This conclusion suggests that future modeling efforts to improve the descriptions of the failure process may be warranted.

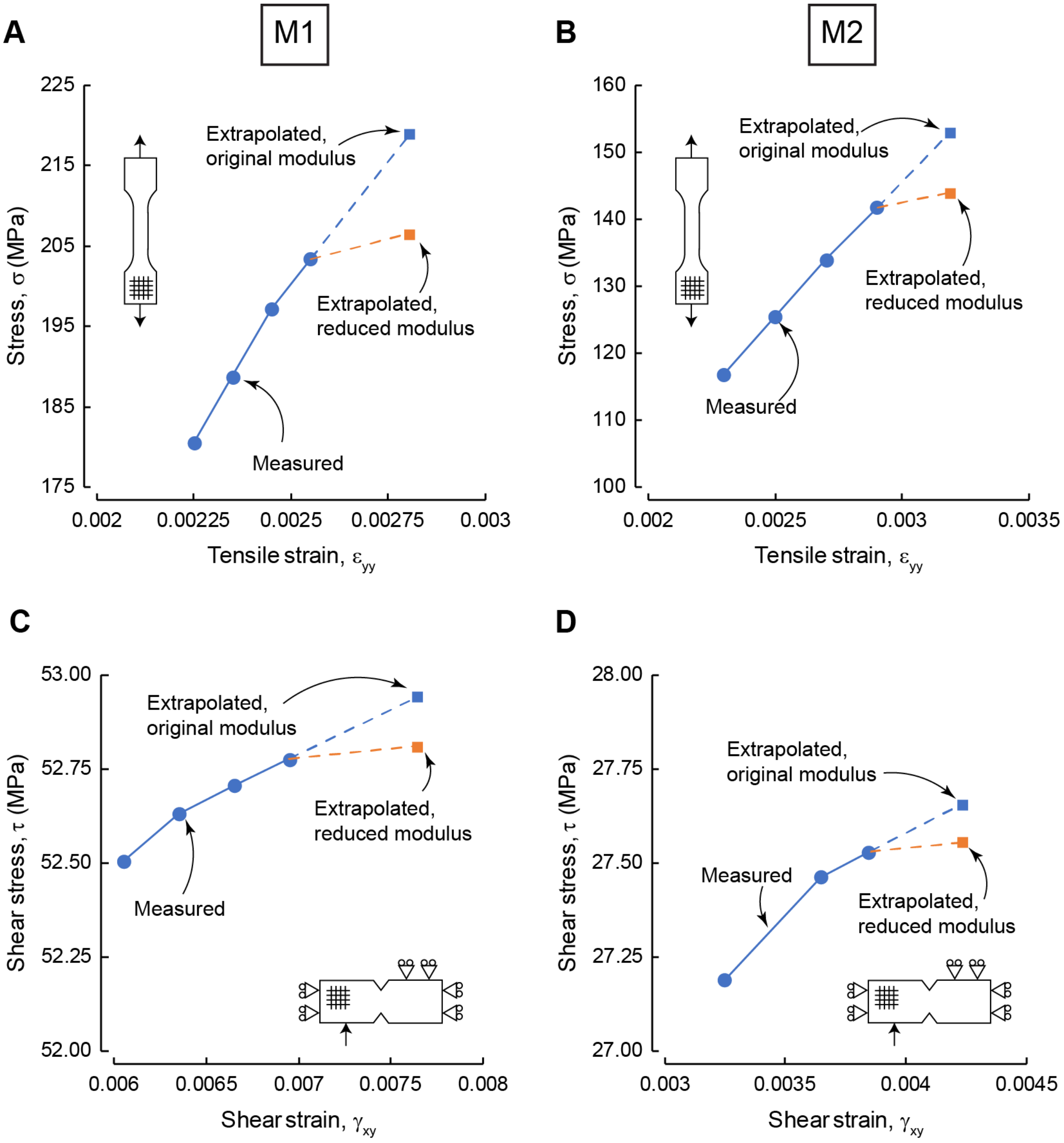

Figure B1. Final points of the stress/strain curves used as inputs in the UMAT of the inelastic model. Originally, points beyond the end of the measured data are extrapolated using the tangent moduli calculated from the final two measured points. This section examines the effect of lower final moduli, produced by adding artificial points beyond the end of the measured data such that the final moduli are reduced by a factor of 5.

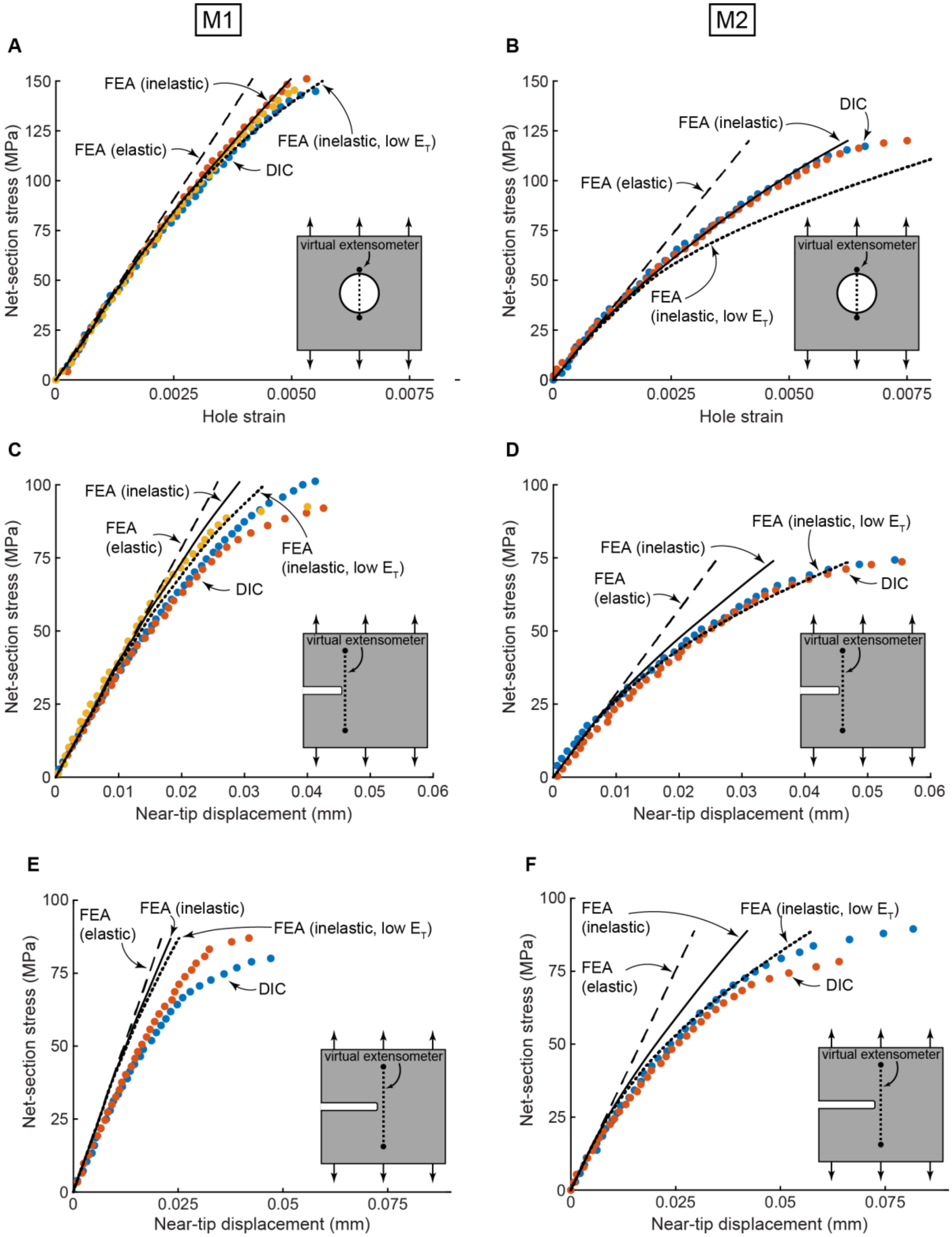

Figure B2. Global responses for open-hole tension edge-notched tension of material M1 (A, C, and E) and M2 (B, D, and F) from measurements (*DIC*) and computed using (i) purely elastic material definitions (*elastic*), (ii) the inelastic model with only measured data in the UMAT (*inelastic*), and (iii) the inelastic model with reduced final tangent moduli of the stress/strain curves used as inputs to the UMAT (*inelastic, low E_T*).

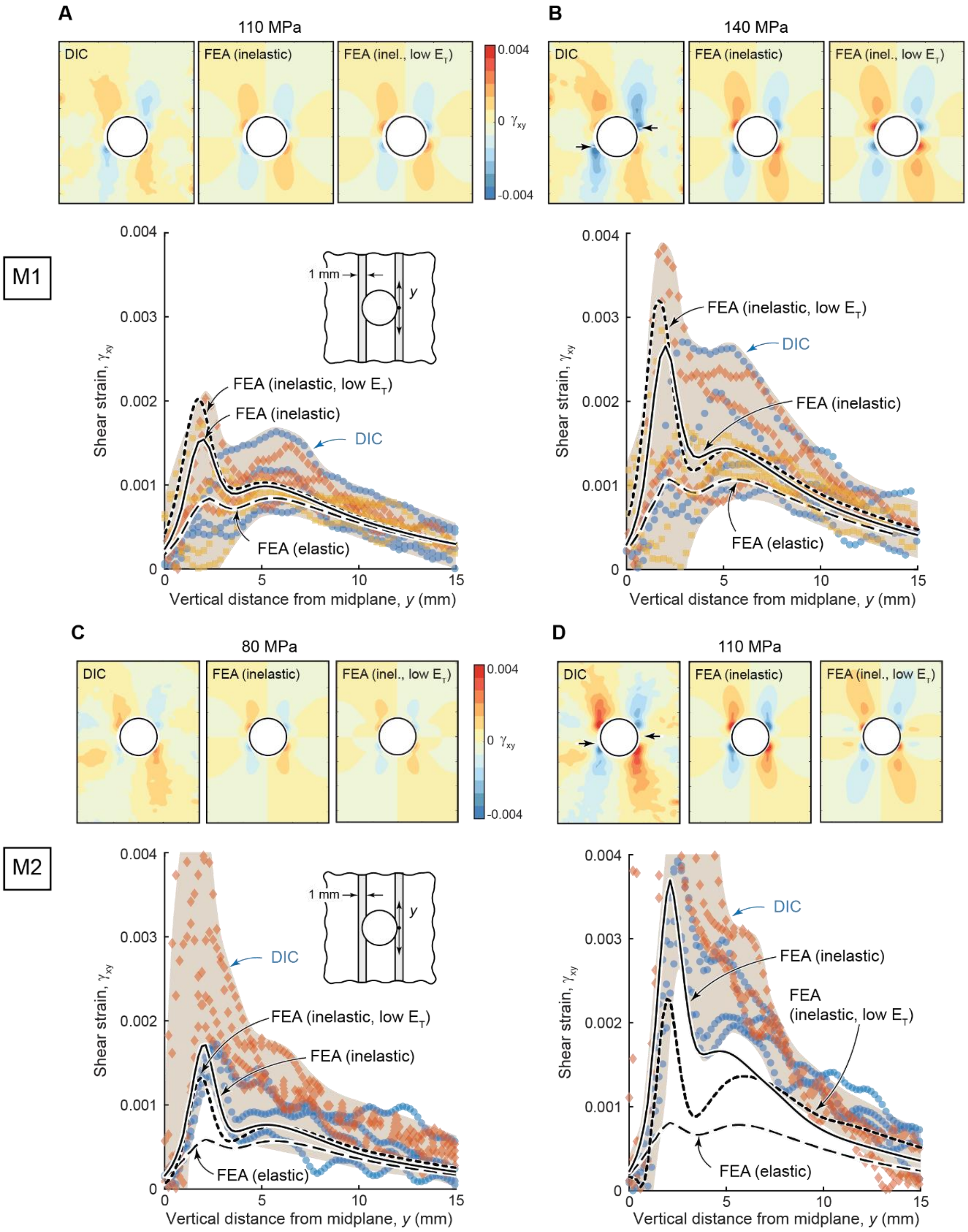

Figure B3. Comparisons of measured and computed shear strains for open-hole tension for material M1 (A, B) and M2 (C, D). The full-field strain maps are a representative measured field and the fields predicted via FEA with the inelastic model without and with reduced tangent moduli in the input curves. The plots show results of line scans, additionally including the results from simulations with the purely elastic model. Shaded bands indicate the range of measured values.

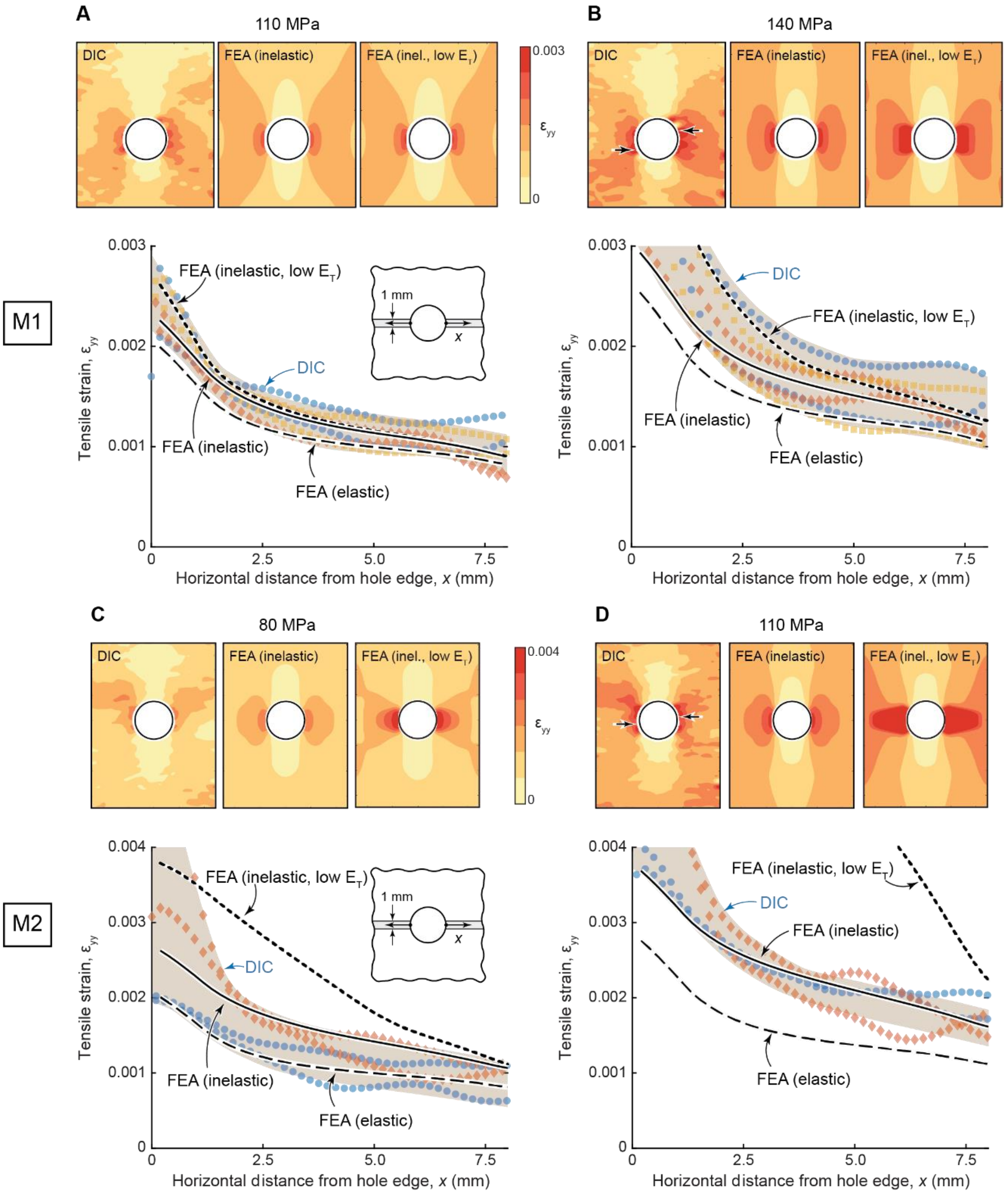

Figure B4. Comparisons of measured and computed tensile strains for open-hole tension for material M1 (A, B) and M2 (C, D).

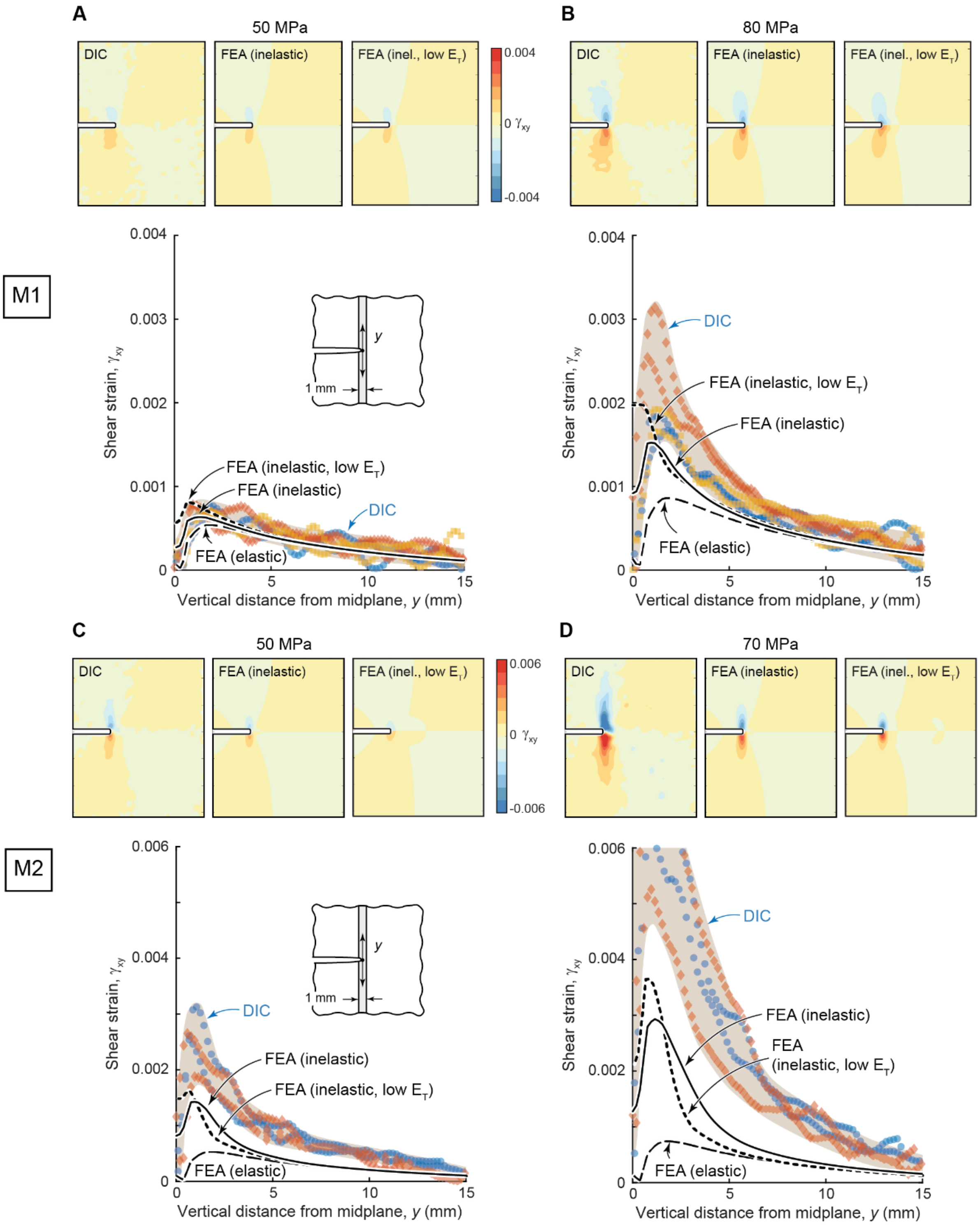

Figure B5. Comparisons of measured and computed shear strains for single-edge notched tension with a/W = 0.3 for material M1 (A, B) and M2 (C, D).

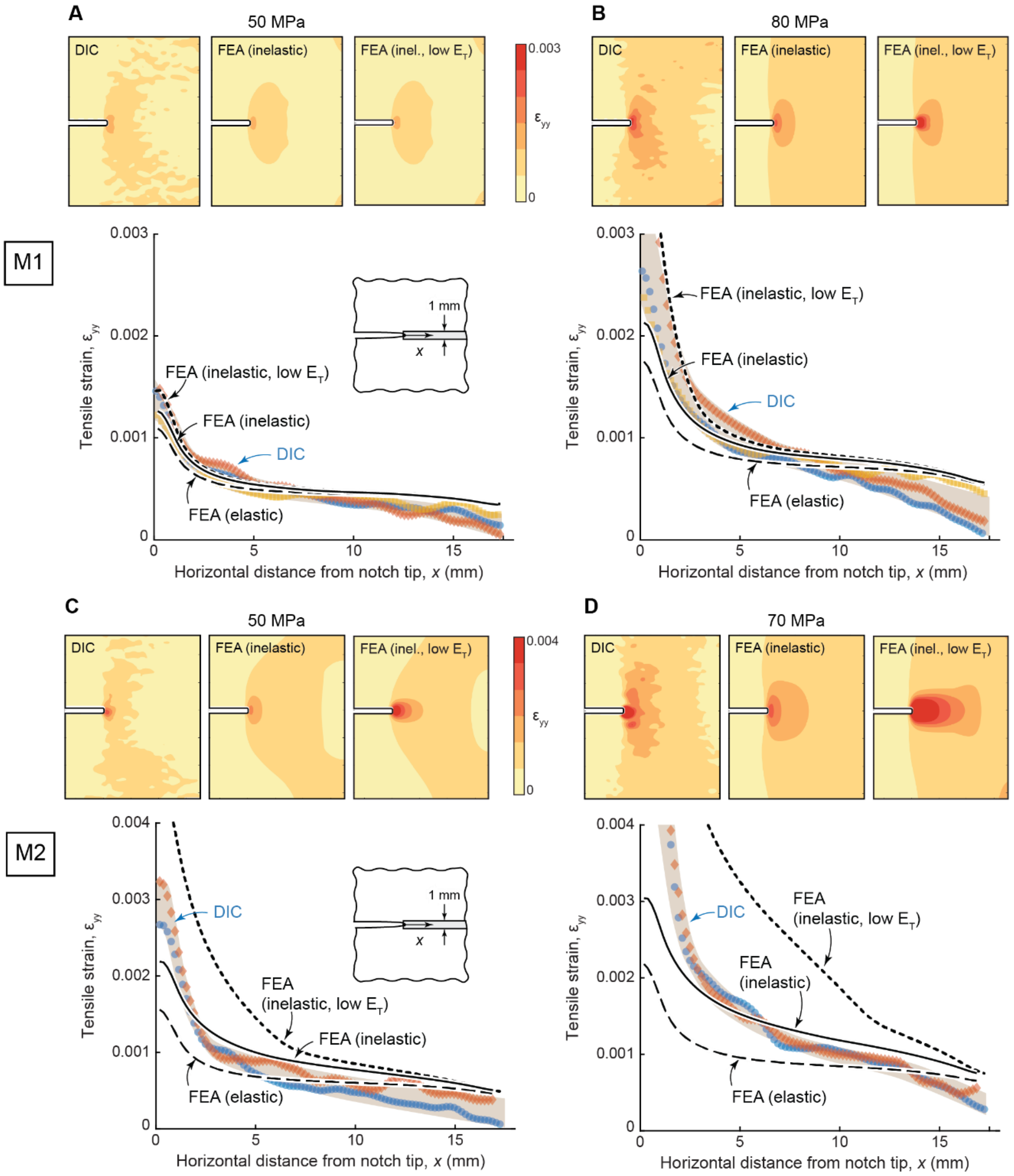

Figure B6. Comparisons of measured and computed tensile strains for single-edge notched tension with a/W = 0.3 for material M1 (A, B) and M2 (C, D).

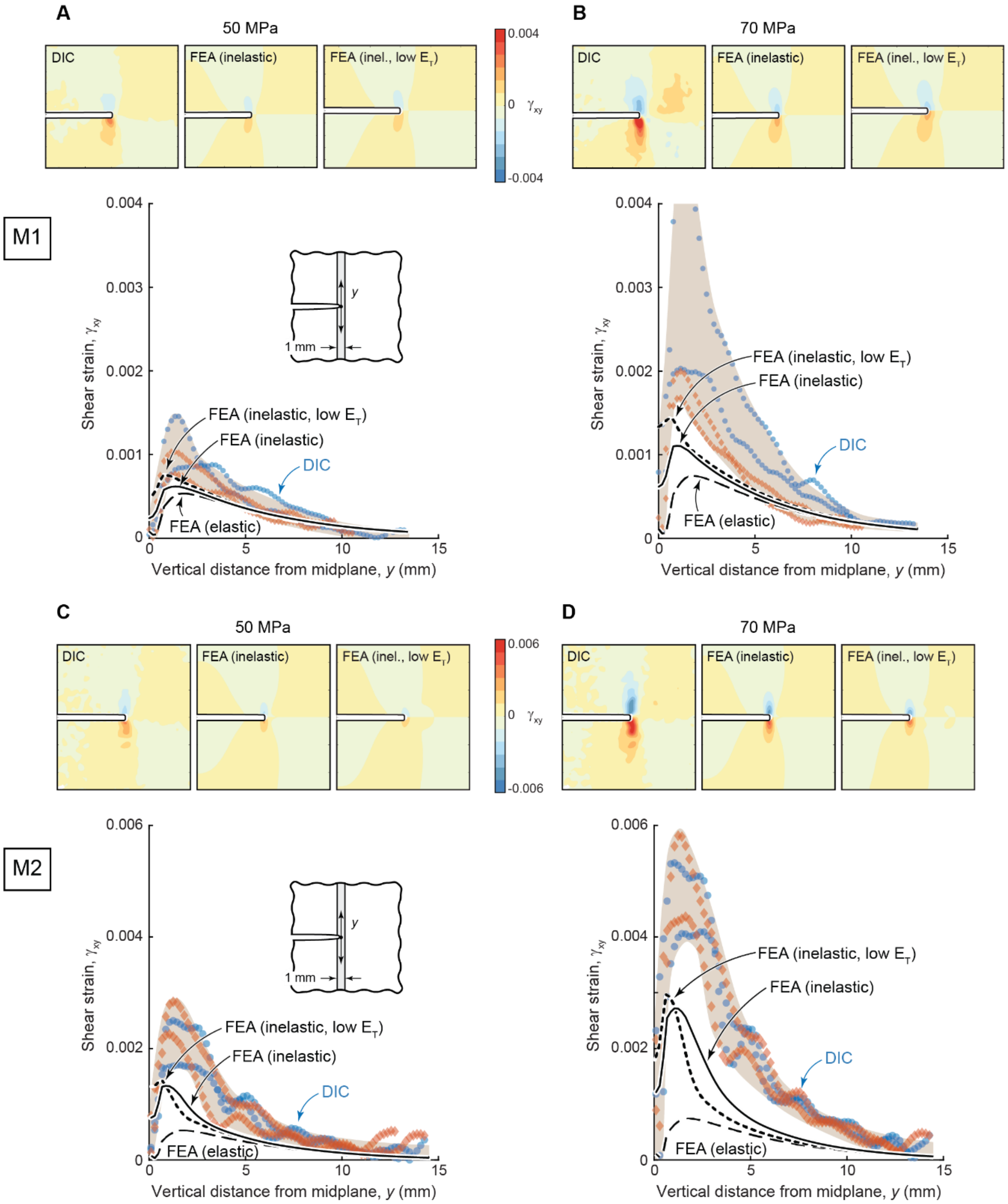

Figure B7. Comparisons of measured and computed shear strains for single-edge notched tension with a/W = 0.5 for material M1 (A, B) and M2 (C, D).

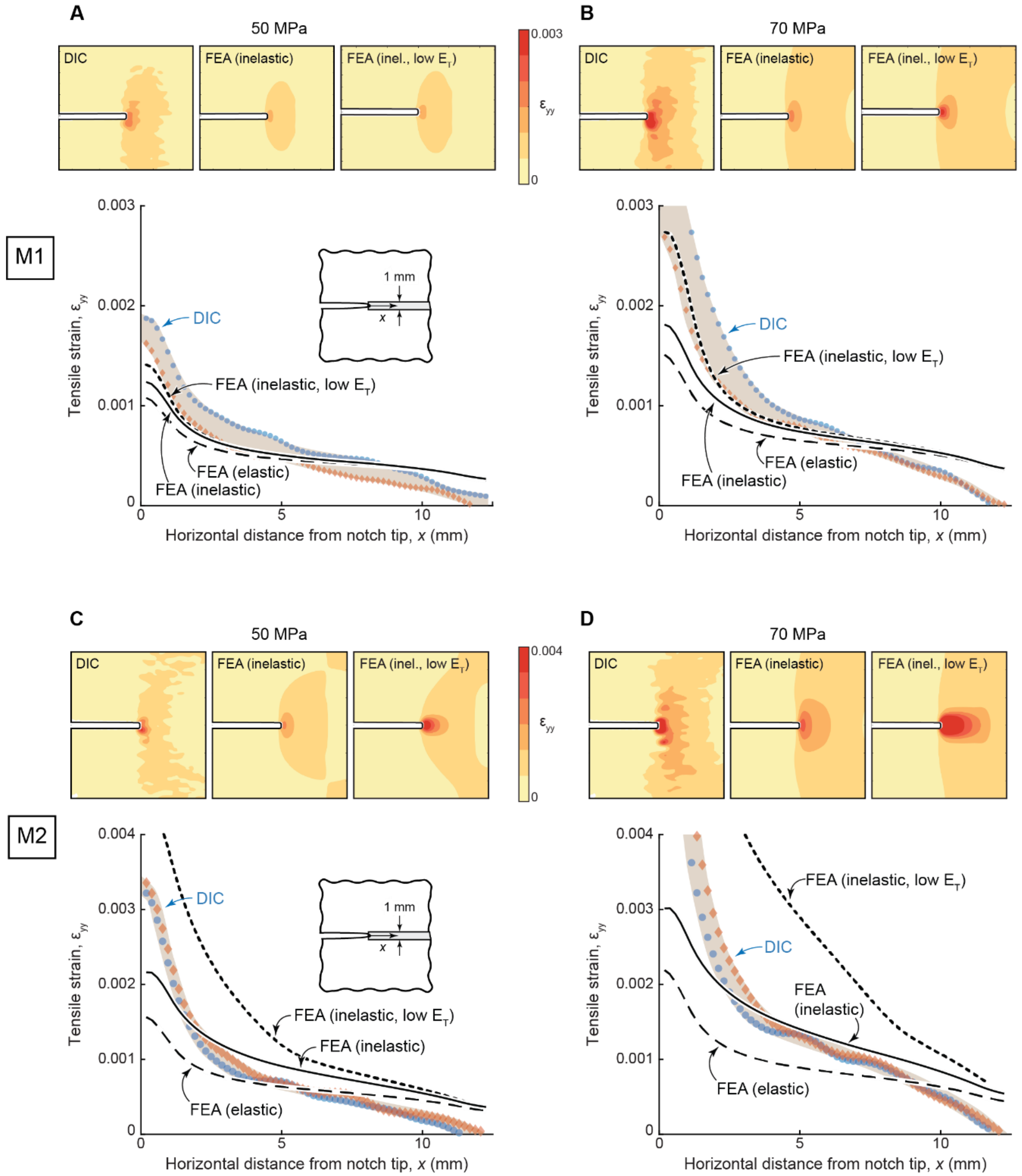

Figure B8. Comparisons of measured and computed tensile strains for single-edge notched tension with a/W = 0.5 for material M1 (A, B) and M2 (C, D).